nature communications

Article

https://doi.org/10.1038/s41467-026-71502-z

Neurons of the human subthalamic nucleus engage with local delta frequency processes during action cancellation

Received: 14 November 2024

Accepted: 23 March 2026

Published online: 21 April 2026

Check for updates

Johanna Petra Szabó[1,2,3], Panna Hegedüs[1,3,4], Tamás Laszlovszky[1,3], László Halász[5], Gabriella Miklós[3,5], Bálint Király[1,6], György Perczel[5], Virág Bokodi[2,7], Lászlo Entz[5,8,9], István Ulbert[5,10,11], Gertrúd Tamás[12], Dániel Fabó[13,14], Loránd Erőss[5] & Balázs Hangya[1,6,15]

The subthalamic nucleus (STN) is a critical hub for inhibitory control, implicated in decision making under conflict and impulsivity. Delta frequency oscillations have also been associated with inhibitory control processes, yet the relationship between human STN neuronal activity and local delta frequencies during response inhibition remains unresolved. Here we recorded STN neurons and local field potentials in patients with Parkinson's disease performing a stop-signal reaction time task during deep brain stimulation surgery. Approximately half of STN neurons responded to a diverse set of behaviorally relevant events including go and stop signals, with stronger go-related firing and enhanced delta phase coupling linked to failed inhibition. Notably, a specific population of bursting STN neurons showed increased delta coupling. These findings suggest that STN neurons integrate go and stop information, and that enhanced delta engagement and bursting may impair inhibitory control, providing insights into the neuronal mechanism of action cancellation.

The hyperdirect pathway, connecting frontal cortical areas including the pre-supplementary motor area and the inferior frontal gyrus with the subthalamic nucleus of the basal ganglia, has been associated with inhibition of motor responses and canceling of actions[1–3]. More generally, it is deeply involved in determining when to act, impacting reaction time, impulsivity and decision making under conflict[4,5].

Frontal cortical slow oscillatory activities were shown to be implicated in decision processes that involve inhibitory control[6–9]. Conflict anticipation, inferred from successful stopping of ongoing actions, was associated with a fronto-central power increase in the 3–5 Hz frequency band[7]. Low-frequency activity related to decision conflicts[10–12] and specifically to action inhibition[13] were also demonstrated in the STN. Importantly, the low-frequency synchronization of

[1]Laboratory of Systems Neuroscience, HUN-REN Institute of Experimental Medicine, Budapest, Hungary. [2]Epilepsy Center, Institute of Neurosurgery and Neurointervention, Semmelweis University, Budapest, Hungary. [3]János Szentágothai Neurosciences Program, Semmelweis University School of PhD Studies, Budapest, Hungary. [4]Department of Pathology, Forensic and Insurance Medicine, Semmelweis University, Budapest, Hungary. [5]Department of Functional Neurosurgery, Institute of Neurosurgery and Neurointervention, Semmelweis University, Budapest, Hungary. [6]Division of Neurophysiology, Center for Brain Research, Medical University of Vienna, Vienna, Austria. [7]Roska Tamás Doctoral School of Sciences and Technologies, Péter Pázmány Catholic University, Budapest, Hungary. [8]Endomin Center, Clinic Hirslanden Zürich, Zürich, Switzerland. [9]MIND Clinic, Budapest, Hungary. [10]Institute of Cognitive Neuroscience and Psychology, HUN-REN Research Centre for Natural Sciences, Budapest, Hungary. [11]Faculty of Information Technology and Bionics, Pázmány Péter Catholic University, Budapest, Hungary. [12]Department of Neurology, Semmelweis University, Budapest, Hungary. [13]Department of Voice, Speech and Swallowing, Semmelweis University, Budapest, Hungary. [14]Department of Neurology, University of Szeged, Szeged, Hungary. [15]Subcortical Modulation Research Group, HUN-REN Institute of Experimental Medicine, Budapest, Hungary. e-mail: balazs.hangya@meduniwien.ac.at

frontal cortex and STN reflected action cancellation and correlated with successful stopping[13]. However, how local neurons of the STN mediate this process has not yet been revealed, hindering a mechanistic understanding of conflict processing in the STN.

To address this, we recorded neuronal spiking activity from the STN while patients with Parkinson's disease performed a stop signal reaction time (SSRT) task. This confirmed the presence of STN spiking related to go and stop cues[2,14], but also demonstrated STN activity predictive of stop performance, violating former assumptions relegating such functions to more downstream circuits[2], while more consistent with others assigning complex functions to STN including action planning[15,16]. Following up on this, we found that increased STN activity after go signals and stronger phase coupling to STN delta band activity hindered patients' ability to stop.

We observed that a large fraction of the recorded units exhibited bursting, which may be related to previous findings that has associated Parkinson's disease (PD) with an increase in bursting activity in the STN[17,18]. A specific subset of strongly bursting units that showed suppressed activity after go signal presentation were more phase coupled to delta activity than weakly bursting units with similar response properties, suggesting that bursting may impair response inhibition via strong engagement with local delta band activity.

Deep brain stimulation (DBS) has been associated with reduced decision thresholds, leading to fast but inconsistent decisions[19,20]. We found that while this was indeed the case in some patients, other patients benefited from DBS surgery not only in their motor functions[21] but also in their cognitive domain in the form of increased rather than decreased reaction times. These patients showed stronger STN bursting and signs of stronger engagement of STN units with local delta band processing, raising the possibility that patients with more severe STN dysfunction may benefit from DBS implantation with respect to their decision making.

Results

Stop signal reaction time task performed by patients with Parkinson's disease

Patients with PD scheduled for DBS implantation surgery were involved in the study (Supplementary Tables S1 and S2). Patients were introduced to the task and performed the first behavioral test during preoperative evaluation on the day before surgery, after 12-h withdrawal of PD medication ($n = 13$; right hand, $n = 13/13$; left hand, $n = 11/13$; preoperative test). Next, patients were tested during DBS surgery, while single and multiunit activity was measured from the STN. Thirteen patients participated in the intraoperative tests during which both the left hemisphere (buttons pressed by right hand) and the right hemisphere were tested in 12–12 patients. Finally, patients with PD enrolled in the study were tested approximately one year (13.1 ± 11.2 months, mean ± SD) post-surgery, after their optimal stimulation parameters were determined by the attending neurologist. The tests were performed after 12-h withdrawal of PD medication, first for the left side (right hand), then for the right side (left hand) in combination with 60-channel EEG recording. Patients were first tested with their DBS stimulator turned off, then the test was repeated with stimulation turned on (DBS-off left hemisphere, $n = 10$; right hemisphere, $n = 12$; DBS-on left hemisphere, $n = 10$; right hemisphere, $n = 5$; postoperative test; Fig. 1a).

To test inhibitory control in patients with PD, they performed a Stop Signal Reaction Time task. Patients viewed visual stimuli on a screen consisting of two integers from {1, 2, 3} presented next to each other (go signal), and they were instructed to press the corresponding buttons in the same order as quickly as they could on a custom-designed button box. After patient response, a feedback screen appeared stating whether the response was correct (over green background), or incorrect (over red background). In part of the trials, the screen featuring the stimuli was followed by a STOP instruction presented at variable delays (stop signal delay, SSD), prompting

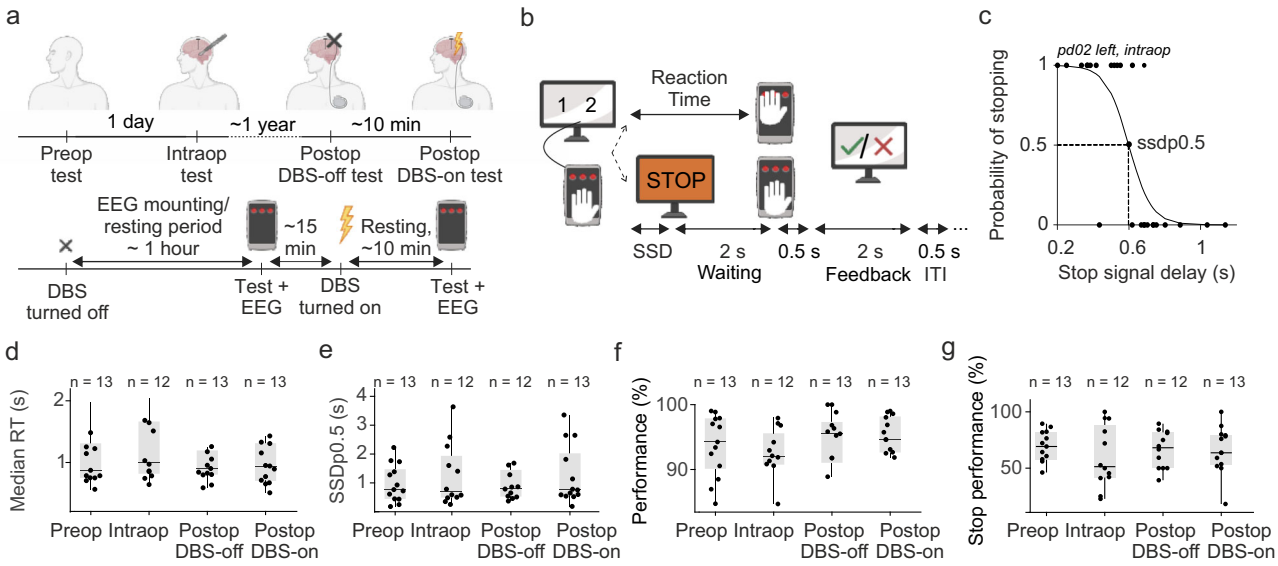

Fig. 1 | Stop Signal Reaction Time Task performed by patients with Parkinson's disease. a Timeline of the experiment. **b** Schematic representation of the Stop Signal Reaction Time (SSRT) paradigm. Two numbers were shown on the screen simultaneously, next to each other (cue). Participants had to press the corresponding buttons (key press) in the correct order on a custom-designed button box. In a subset of trials, the cue was followed by a stop signal with variable delay (stop signal delay, SSD), when the key press had to be withheld. **c** A generalized linear regression model was fitted to the SSDs corresponding to successful (1) and failed (0) stop trials to estimate the SSD with 50% probability of successful stopping (SSDp0.5, shown in an example patient). Median RTs (**d**, $n = 13$, $n = 12$, $n = 13$, $n = 13$), SSDp0.5 values (**e**, $n = 13$, $n = 12$, $n = 12$, $n = 13$), task performance (percentage of correct no-stop trials, **f**, $n = 13$, $n = 12$, $n = 13$, $n = 13$), stop performance (percentage of successful stop trials, **g**, $n = 13$, $n = 12$, $n = 12$, $n = 13$) in preoperative, intraoperative and postoperative experiments. Each dot represents the data of one patient (left side session). Box plots represent median, interquartile range, and non-outlier range. Outliers are not shown for better visualization; see Supplementary Fig. S1 for all data. Source data are provided as a Source Data file. Panels **a**–**b** created in BioRender. Szabó, J. (2026) https://BioRender.com/7tjaoyp.

patients to withhold button pressing (see Supplementary Table S3 for average SSD values). If patients failed to withhold motor response, a feedback screen over red background informed them about the unsuccessful stopping. In case patients managed to refrain from pressing during a 2-s response window, a feedback screen over green background reinforced successful stop response (Fig. 1b; see Supplementary Table S4 for trials numbers).

Behavioral performance in the SSRT task

We measured patients' reaction times (RT) and the estimated SSD that resulted in 50% probability of successful response inhibition (SSDp0.5; Fig. 1c). Both RT and SSDp0.5 showed considerable variation within and across patients and no systematic differences were seen in these parameters among pre-, intra- and postoperative tests including DBS-on and DBS-off measurements (Fig. 1d–e), except for an intraoperative slowing in some of the patients that was significant when testing the right side (Supplementary Fig. S1e–f).

We also tested task performance (percent correct button presses) and stop performance (proportion of correct stops compared to all stop trials). While task performance was over 60% in 96 of 104 (92.3%) tests, it showed substantial heterogeneity without consistent changes from pre- to intra- to postoperative tests (Fig. 1f–g), except for an intraoperative drop of performance (Supplementary Fig. S1g).

Patients were categorized based on their clinical phenotype into tremor-dominated (TD; $n = 5$), akinetic-rigid (AR; $n = 6$) and mixed (MX; $n = 2$) groups. Tremor-dominated patients showed longer reaction times in preoperative tests, and this difference appeared to be reduced after DBS surgery; however, these differences were not significant at this sample population size (Supplementary Fig. S2).

Unified Parkinson's disease rating scale (UPDRS) scores, measuring PD severity, were determined both with (med-on) and without medication (med-off) preoperatively and postoperatively. These correlated positively with RT (significant for med-on in preoperative tests, both sides and for med-on and med-off postoperative DBS-on tests for the right side) and SSDp0.5 (significant for med-on and med-off postoperative DBS-on tests for both sides; Supplementary Fig. S3), suggesting that more advanced disease stages were associated with longer reaction times.

Frontal and STN delta power increased during SSRT performance

Inhibitory control during response withholding involves top-down cortical processes[22,23]. We sought for task-related changes in cortical processing during SSRT performance by aligning postoperative DBS-off EEG spectrograms to visual go signal and stop signal onsets (event-related spectrograms, ERS). We found an increase in delta band (1–4 Hz) power around go signals (Fig. 2a), which continued after stop signals in the stop trials (Fig. 2b), indicating increased frontal delta band activity during SSRT performance.

When we compared stop trials in which the patient was successful in withholding response with unsuccessful stop attempts, we found that failed stops were associated with significantly lower right frontal (F4 channel) delta power after go signals (Fig. 2c) and lower left central (CP1 channel) delta power before stop signals (Fig. 2d). This may suggest that delta power increase in these regions contributes to better inhibitory motor control (Fig. 2).

Similar tendencies were observed with DBS stimulation turned on, although frontal-central delta increase was smaller in magnitude and shorter in duration and started earlier (Supplementary Fig. S4a–b), in line with a proposed reduction of inhibitory control during subthalamic stimulation[19]. Successful response inhibition was associated with higher delta band activity before the stop signal (C3 channel), consistent with DBS-off recordings (Supplementary Fig. S4c–d).

Beta band power showed a marked decrease following the go signal (Supplementary Fig. S4h) and an increase after the stop signal, mainly in the fronto-central region (Supplementary Fig. S4i). Higher frontal beta was associated with successful action cancelation (Supplementary Fig. S4j-k).

Having revealed delta band power changes in frontal EEG associated with the SSRT, we asked whether there were concomitant changes in delta band power in the STN local field potential (LFP). Therefore, we calculated event-triggered LFP averages (ETA, Fig. 3a, Supplementary Fig. S5a) and ERS of STN LFP power (Fig. 3b, Supplementary Fig. S5b) using the intraoperative microelectrode recordings performed during DBS surgery. We found that STN delta band power increased around go signal presentation (Fig. 3a,b), similar to what we found for frontal EEG channels in the postoperative DBS-off recordings. Moreover, this delta power increase was correlated with faster patient reactions, suggesting that go signal-related STN delta power increase facilitates cue detection and/or response preparation (Fig. 3c). In contrast, stop signals were followed by a decrease in delta power (Supplementary Fig. S5b). We did not find significant differences in delta band power in the STN when we compared successful and unsuccessful stop attempts (Supplementary Fig. S5c).

Next, we tested whether delta band activity changes were coordinated across frontal cortex and STN. For this, we used bipolar frontal EEG recordings obtained during DBS surgery. Interestingly, delta band coherence markedly decreased around go signal presentation (Fig. 3d) but increased right after stop signals (Supplementary Fig. S5d–e). Decreased delta coherence around go signals correlated with faster go responses (Fig. 3e). Nevertheless, successful response withholding was associated with higher frontal cortex-STN delta band coherence before (Fig. 3f), but lower after stop signals (Supplementary Fig. S5f). These results confirm that go signal detection and response do not rely on the hyperdirect pathway, in contrast with response inhibition[13].

STN neurons respond to behaviorally relevant events during SSRT

We recorded $n = 193$ units from the STN of 13 patients while they performed the SSRT task. Of these, $n = 48$ were considered single neuron activity (SUA) based on conservative cluster quality criteria (ID > 15 and L-ratio <0.02; see Methods), while the others were considered multiunits (MUA). Their localization within the STN was determined based on the postoperative reconstruction of the microelectrode tracks (Fig. 4a–e).

We found that many of these units responded to behaviorally relevant task events. First, we aligned spiking activity to go signals and calculated event-aligned raster plots and peri-event time histograms (PETH). These revealed that 22% of the recorded units changed their spike rate upon go signal presentation, with an equal portion of activated ($n = 22$, 11%) and inhibited ($n = 20$, 10%) units (Fig. 4f). When we separated the activity of go signal-responsive units in stop trials based on whether the patient was successful in inhibiting the motor response, we found that failed attempts were preceded by a significantly larger go-elicited activation (Fig. 4g).

When we aligned unit activity to the stop signals, we found an 8% of units responding significantly to stop signal presentation: $n = 5$ (3%) of units were activated, while $n = 9$ (5%) showed inhibition (Fig. 4h). Although the percentages of significantly activated and inhibited neurons after stop signals were smaller than those after the go signals, this could also be due to the lower statistical power in the former analysis given that only a subset of trials were stop trials. Nevertheless, these relatively low numbers were significantly higher than what was expected by chance (based on the binomial distribution model, the probability of observing $n = 14$ or more stop-responsive units was 0.0442), and quantile-quantile plots indicated that those neurons determined as responsive had substantially lower p-values than expected by chance (Supplementary Fig. S6a-b).

The average PETHs indicated firing rate changes already before the stop signals, suggesting that at least some of these units were

https://doi.org/10.1038/s41467-026-71502-z

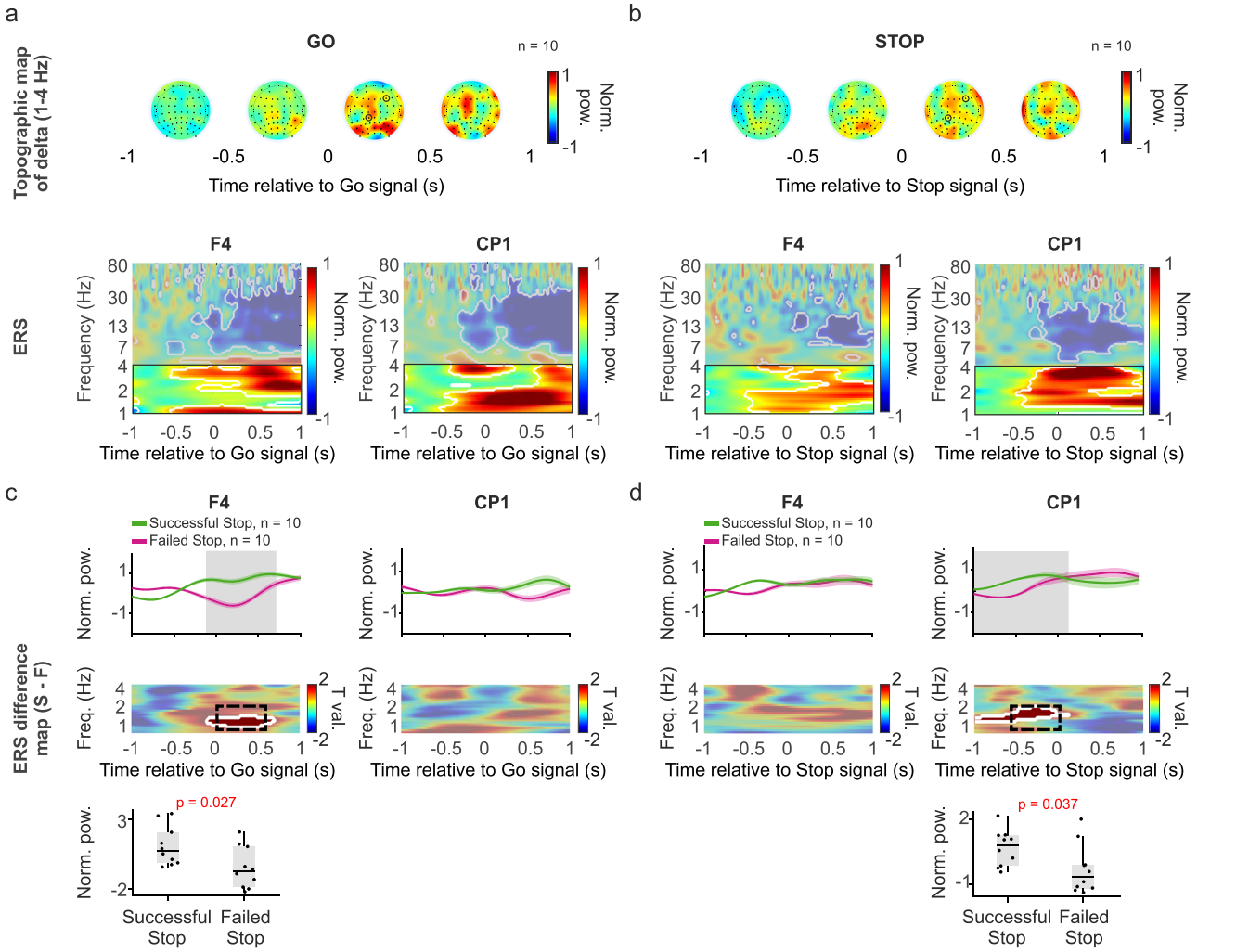

Fig. 2 | Frontal delta power increased during SSRT performance. a Top, topographical maps (topo plots) of 60-channel EEG recordings showing delta (1–4 Hz) power derived from scalp current densities, averaged across trials and patients ($n = 10$) in 0.5 s time windows aligned to go signals. Baseline (−1 -0.5 s) normalization was applied on z-scored data, averaged across patients. Black dots, position of EEG electrodes in the standard 10–20 system. Data from left side postoperative DBS-off measurements are shown. Bottom, event-related spectrograms (ERS) of selected channels (marked by black circles on the topo plots) aligned to go signals (delta frequency range highlighted). White contours indicate significant changes from baseline (two-sided permutation test with cluster-based correction, $p < 0.05$). **b** The same as in panel **a** but aligned to stop signals ($n = 10$). Frontal and centro-parietal delta power increase was detected both around go and stop signals. **c** Top, delta band spectral power averages aligned to go signals for successful (green) and failed (pink) stop trials, averaged across trials and patients ($n = 10$) from left side postoperative DBS-off measurements, shown for the same channels as in panel **a** (line and shading, mean ± SE). Baseline (−1 −0.5 s) normalization was applied on individual patient averages. Significant differences are marked by gray shading ($p < 0.05$, two-sided permutation test with cluster-based correction). Middle, spectrograms displaying delta power differences between successful and failed stop trials, represented as paired T statistics (T val.) for each time-frequency point. Significant changes relative to baseline are indicated by white contours (two-sided permutation test with cluster-based correction, $p < 0.05$). Bottom, delta power difference between successful and failed stop trials, calculated for the time-frequency windows marked in the middle panel (black dashed box). Box-whisker plots show median, interquartile range and non-outlier range. $p = 0.027$, two-sided Mann–Whitney U-test. **d** The same as in panel **c** but aligned to stop signals ($n = 10$). Successful stop trials were associated with larger delta power after the go cue and before the stop cue. $p = 0.037$, two-sided Mann–Whitney U-test. Source data are provided as a Source Data file.

affected by the go signals, with their firing rate changes continuing or accentuated after the stop signals. In line with this, Stop-activated units showed higher firing rate for failed stop attempts before the stop signals (Fig. 4i), potentially corresponding to similar differences found for Go-activated units (Fig. 4g, Supplementary Fig. S7d).

Following up on this, we found units that showed differential activity before successful and unsuccessful motor inhibition, thus predicting the outcome of stopping (Fig. 4j). In $n = 9$ units (5%), activity was higher before failed stop attempts (type 1 predictive units), whereas in the case of $n = 5$ units (3%) we found the opposite, that is, faster spiking before successful motor inhibition (type 2 predictive units). Thus, type 1 predictive units were consistent with the differential responses to go signals in failed vs. successful stop trials shown above.

Next, we tested spike rate changes around key presses by aligning spike rasters and PETHs to the first button press of patients in each trial. We found that 36% of all units responded significantly to button press, with a dominance of activation ($n = 44$, 23%) over inhibition ($n = 25$, 13%; Supplementary Fig. S6c).

Finally, some of the recorded units (17%) responded to behavioral feedback and increased ($n = 16$, 8%) or decreased ($n = 17$, 9%) their firing upon presentation of the feedback screen (Supplementary Fig. S6d). However, upon closer inspection, the feedback-activated units seemed to show an activation that already started earlier and

https://doi.org/10.1038/s41467-026-71502-z

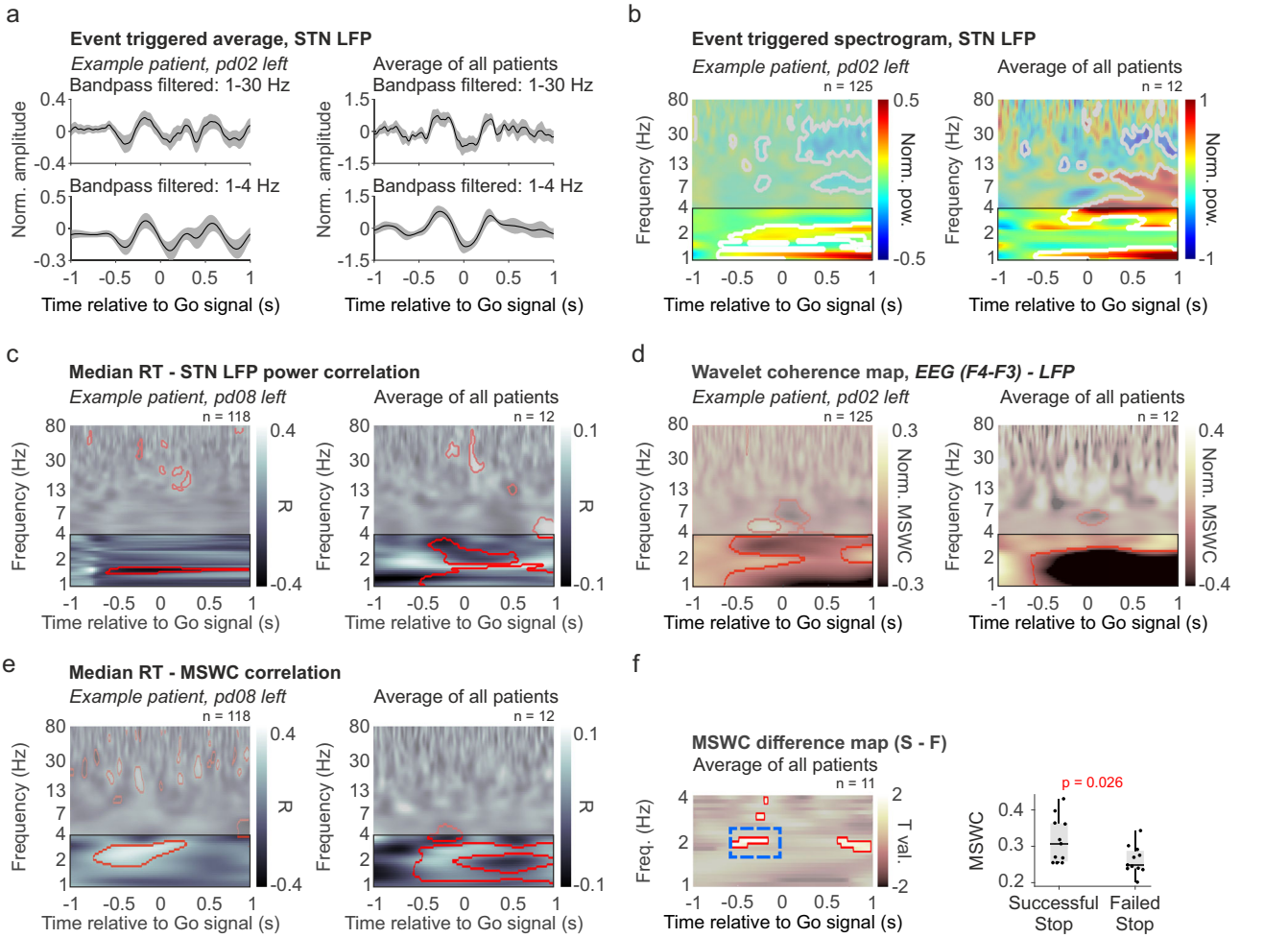

Fig. 3 | STN delta power increased during SSRT performance. a Event-triggered averages (ETA) of intraoperative STN LFP aligned to go signals. Top, broadband (1–30 Hz); bottom, delta band (1–4 Hz). Shading, SE. Left, example patient; right, average ($n = 12$ patients). **b** Event-related wavelet power spectrograms (ERS) relative to baseline, aligned to go signals. Delta band is highlighted. White contours mark significant changes from baseline (−1 to −0.5 s). Left, example patient ($n = 125$ trials); right, average ($n = 12$ patients). **c** Time-frequency correlation of RT and STN LFP power around the go signal (Pearson's r, within-subject). Left, example patient ($n = 118$ trials); red contours indicate significant correlations across trials (two-sided t-test, $p < 0.05$). Right, average within-subject correlation maps ($n = 12$ patients); red contours indicate significant changes from baseline (two-sided permutation test with cluster-based correction, $p < 0.05$). **d** Magnitude-squared wavelet coherence (MSWC) of STN LFP and intraoperative frontal bipolar EEG aligned to go signals. Colors represent increases (white) and decreases (black) relative to baseline (−1 to −0.5 s). Delta band is highlighted. Red contours mark significant changes from baseline. Left, example patient ($n = 125$ trials); right, average ($n = 12$ patients). **e** Time-frequency correlation of RT and MSWC around the go signal (Pearson's r, within-subject). Left, example patient ($n = 118$ trials); red contours indicate significant correlations across trials (two-sided t-test, $p < 0.05$). Right, average within-subject correlation maps ($n = 12$ patients); red contours indicate significant changes from baseline (two-sided permutation test with cluster-based correction, $p < 0.05$). **f** Left, MSWC difference between successful and failed stop trials, aligned to go signals, expressed as paired T statistics (T val.) calculated for each time-frequency point and averaged across patients ($n = 11$). White indicates greater coherence for successful stop trials (two-sided permutation test with cluster-based correction, $p < 0.05$); red contours mark significant clusters. Right, MSWC difference between successful and failed stop trials within the marked window (blue dashed box). Box-whisker plots show median, interquartile range and non-outlier range. $p = 0.026$, two-sided Mann–Whitney U-test. Source data are provided as a Source Data file.

seamlessly continued after the feedback presentation, rather than a discrete increase at feedback onset, potentially representing feedback-anticipation.

Altogether, 52% ($n = 100$) of all units responded to at least one event (including predictive units), demonstrating an active engagement of the human STN during SSRT performance (Fig. 4k; separate analyses of SUA and MUA activities revealed largely similar results, Supplementary Fig. S7). The direction of go signal and key press responses were always concordant among units, whereas many STN units lacking significant go signal-elicited firing rate changes still responded to key presses, mostly by activation (Fig. 4l).

Most recorded units were localized to the motor part of STN ($n = 85$, 44%), with a smaller fraction in the associative part ($n = 23$, 12%) and only a few units were recorded in the limbic part ($n = 3$, 2%), whereas localization to identified parts of the STN nucleus could not be reliably carried out for $n = 82$ units (units close to STN boundaries, Supplementary Fig. S6e). Responsive or predictive units largely followed this distribution, with $n = 52$ units (52%) localized to the motor part of STN and $n = 14$ units (14%) localized to the associative part (Fig. 4m; Supplementary Fig. S6f).

STN neurons were phase coupled to local delta activity, especially before unsuccessful stop attempts

We demonstrated that when the patients were presented with the go signal, a significant fraction of STN units responded and, in parallel, delta power was increased in the STN LFP. We found that these two signatures of a change in activity were not independent, but a large fraction of units showed significant phase coupling (PC) to local delta

https://doi.org/10.1038/s41467-026-71502-z

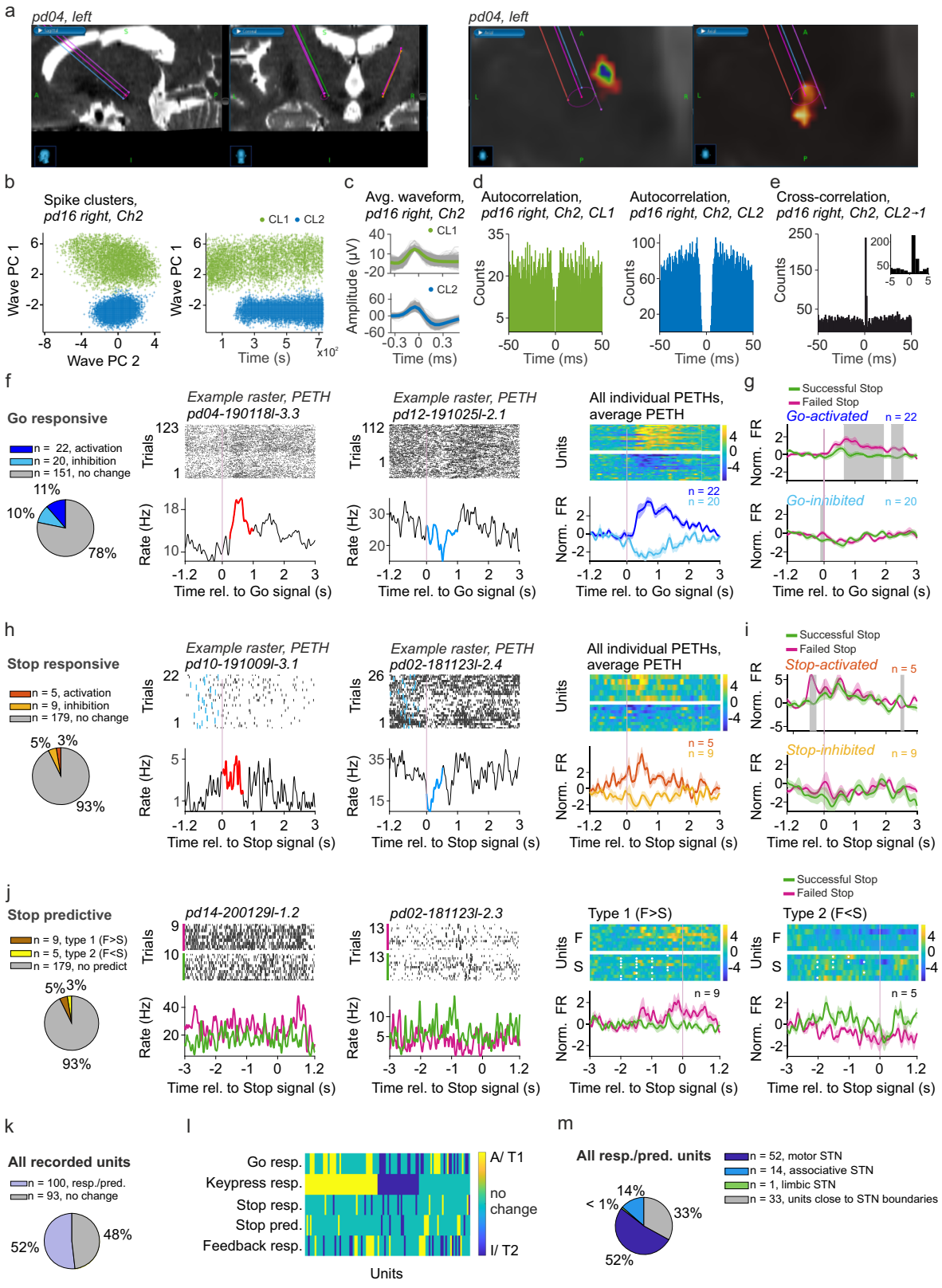

band LFP activity both around the go (Fig. 5a–e) and the stop signals (Fig. 5f–j; Supplementary Fig. S8a–b; single-units were more coupled than multi-units, $p = 0.003$, Fisher exact test, Supplementary Fig. S7e).

The recorded STN units showed delta phase preference also on the population level, most units being locked slightly before the peak of delta around the go signal (mean angle, 1.3 (74.5°); $p = 0.0005$, Rayleigh's Z-test; Fig. 5b, c, Supplementary Fig. S7f) and to the ascending slope around the stop signal (mean angle, 0.33 (18.9°); $p = 0.0333$, Rayleigh's Z-test; Fig. 5g, h). The preferred phase was not significantly different in successful vs. unsuccessful stop trials, neither around the go cue ($0.1 < p < 1$, Watson's two sample test of homogeneity; Fig. 5d left, Supplementary Fig. S7f), nor around stop signals ($0.05 < p < 0.1$, Watson's two sample test of homogeneity; Fig. 5i left).

https://doi.org/10.1038/s41467-026-71502-z

Fig. 4 | STN neurons respond to behaviorally relevant events during SSRT. **a** Left, CT-MR-based reconstruction of microelectrode trajectories in a patient. Right, DTI-based position estimations within STN. Multicolor patches, associative; red, motor subregion. **b** Example spike clusters (CL). Left, first two principal components of spike waveforms (Wave PC1, PC2). Right, PC1 over time. **c** Average waveforms of the same clusters (gray, individual spikes). **d** Autocorrelograms of the same clusters. **e** Crosscorrelogram of the same clusters. Inset, central bins enlarged. **f** Left, proportion of Go-responsive units. Middle, event-aligned raster plots and PETH for representative activated (red) and inhibited (blue) units. Right, heatmaps of the Z-scored PETHs of all Go-responsive units (yellow, increase; blue, decrease) and mean PETHs of activated ($n = 22$) and inhibited ($n = 20$) units (shading, SE). Responsiveness was tested in a 1 s post-event window; larger windows are shown for visualization. **g** PETHs of Go-activated ($n = 22$) and Go-inhibited ($n = 20$) units in successful (green) and failed (pink) stop trials (shading, SE). Gray, significant differences ($p < 0.05$, two-sided permutation test with cluster-based correction). **h** Stop-responsive units. Same layout as in **f**. **i** PETHs of Stop-activated ($n = 5$) and Stop-inhibited ($n = 9$) units. Same layout as in **g** (shading, SE). **j** STN units predictive of stop trial outcome. Left, proportion of predictive units. Middle, raster plots and PETHs for representative type 1 and type 2 units (lower vs. higher activity preceding successful stop, $n = 9$ vs. $n = 5$, respectively). Right, Z-scored PETHs of all Stop-predictive units (yellow, increase; blue, decrease) with average PETHs partitioned according to stop trial outcome (shading, SE). White dots mark windows of significant successful vs. failed trial differences, e.g., at −2 s for a 2 s pre-stop window. Most effects were present within −1 to 0 s. **k** Proportion of behaviorally responsive and/or predictive units. **l** Event-related activity changes of responsive/predictive units. Yellow, activated (A) and type 1 (T1) units; blue, inhibited (I) and type 2 (T2) units. **m** Distribution of responsive/predictive units across STN subregions. Source data are provided as a Source Data file.

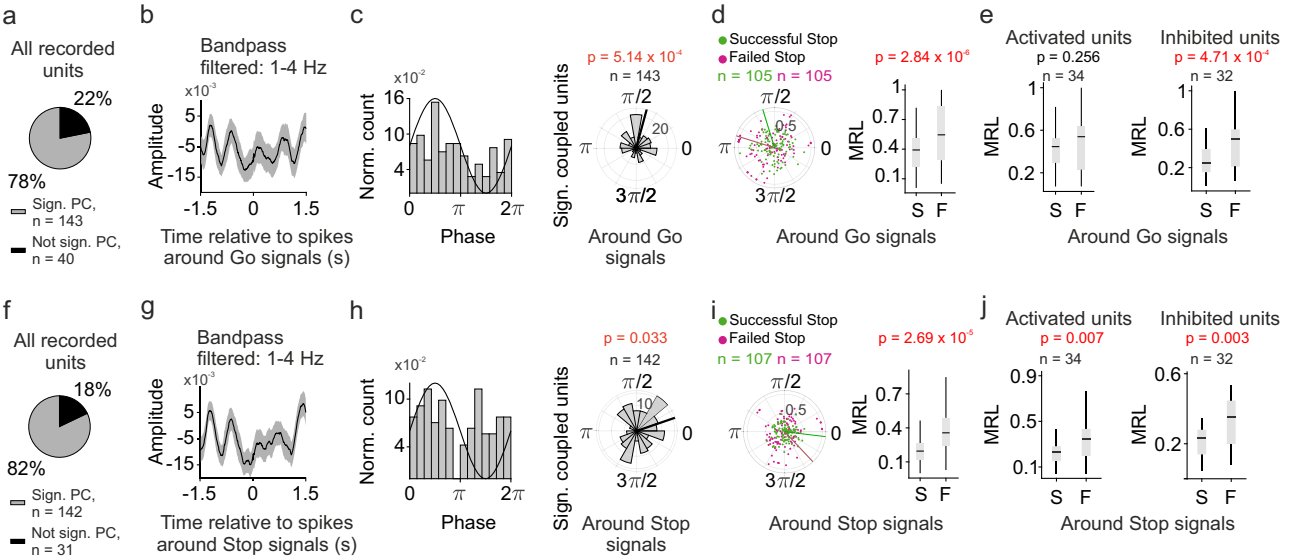

Fig. 5 | STN neurons were phase coupled to local delta activity, especially before unsuccessful stop attempts. **a** Proportion of units significantly coupled to local delta oscillation from all recorded units. Phase coupling was calculated for a -1.5 to 1.5 s window around go signals. **b** Spike-triggered average of delta band (1-4 Hz) LFP, averaged across delta-coupled units for spikes −1.5 s to 1.5 s relative to go signals. Gray shading indicates SE. **c** Left, population phase histogram showing the distribution of preferred phases of delta-coupled units ($n = 143$). Right, rose diagram of the same distribution. Circular uniformity was tested with Rayleigh's test. **d** Left, preferred phase and coupling strength (MRL) of delta-coupled units in stop trials, shown for successful (green, $n = 105$) and failed (pink, $n = 105$) stop attempts. Right, comparison of coupling strength in successful (S) and failed (F) stop trials. Box-whisker plots show median, interquartile range and non-outlier range. $p = 2.84 \times 10^{-6}$, two-sided Mann–Whitney U-test. Outliers are not shown for better visualization; see Supplementary Fig. S8 for all data. **e** Comparison of coupling strength between successful and failed stop trials in different behaviorally responsive (activated, $n = 34$; inhibited, $n = 32$) populations (two-sided Mann–Whitney U-test). Box-whisker plots show median, interquartile range and non-outlier range. Outliers are not shown for better visualization; see Supplementary Fig. S8 for all data. **f**–**j** Same as in panels **a**–**e** but calculated for delta-coupled units ($n = 142$), activated ($n = 34$) or inhibited ($n = 32$) in a −1.5 s to 1.5 s time window around stop signals (successful and failed stop attempts, $n = 107$ each; two-sided tests). Source data are provided as a Source Data file.

We measured delta PC strength of STN units by calculating the mean resultant length (MRL[24]). STN units showed stronger STN delta-coupling associated with failed stop attempts, both measured around the go ($p = 2.84 \times 10^{-6}$, Mann–Whitney U-test; Fig. 5d right, Supplementary Fig. S7f, S8c, e) and the stop signal ($p = 2.69 \times 10^{-5}$, Mann–Whitney U-test; Fig. 5i right, Supplementary Fig. S8d, e). This difference was especially large for units responding with inhibition to go signals (Fig. 5e, j; see also in keypress-responsive units, Supplementary Fig. S8f). Using the go and stop signals as window boundaries and recalculating these analyses in 2 s windows before and after the go signal and after the stop signal yielded similar results (Supplementary Fig. S9).

Trials with a 3-1 stimulus sequence can be considered as high conflict trials due to the inverted order and the skipped button. In those patients where 3-1 stimuli were associated with slower RT compared to low conflict 1-2 stimuli ($n = 3$), high conflict trials were associated with lower delta PC strength (Supplementary Fig. S8g), in line with lower coupling strength observed in successful stop trials.

Since we demonstrated frontal cortex – STN coherence in the delta band that was larger around the go signals preceding successful stops (Fig. 3d–f), we next tested if delta band phase locking could also be detected around the go signals between STN units and frontal cortex EEG (Fig. 6a). We found a significant population level phase locking only before successful stops, suggesting a stronger frontal influence that could reflect hyperdirect pathway activity at the cellular level in the STN (Fig. 6b). At the same time, individual STN neurons showed larger MRL and thus stronger phase locking before failed stops, similar to what was found locally in the STN. However, the stronger phase locking at the individual cellular level did not result in population phase preference due to the near-uniform spread of preferred phases over the circle, in line with the lower frontal-STN coherence during failed stops. Neither of these differences were present around the stop signals (Fig. 6c–d, Supplementary Fig. S8h), again

https://doi.org/10.1038/s41467-026-71502-z

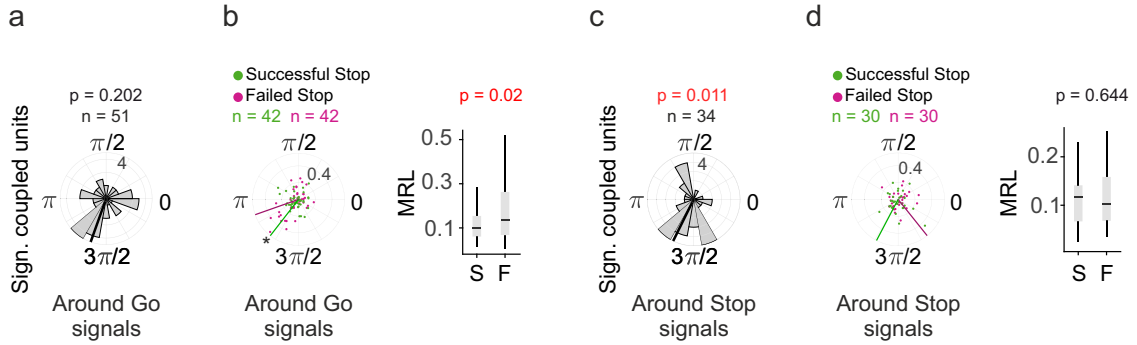

Fig. 6 | STN neurons showed significant population level phase locking to frontal delta before successful stops. a Rose diagram of population phase histogram showing the distribution of preferred phases of units coupled to frontal delta, calculated for spikes in a −1.5 s to 1.5 s time window around go signals. Circular uniformity was tested with two-sided Rayleigh's test ($p = 0.202$). **b** Left, preferred phase and coupling strength (MRL) of frontal delta-coupled units ($n = 51$) in stop trials, shown for successful (S, green, $n = 42$) and failed (F, pink, $n = 42$) stop attempts. Circular uniformity was tested with Rayleigh's test (successful stops, $p = 0.013$; failed stops, $p = 0.194$; two-sided test). Right, comparison of coupling strength in successful (S) and failed (F) stop trials. Box-whisker plots show median, interquartile range and non-outlier range. $p = 0.02$, two-sided Mann–Whitney *U*-test. **c**–**d** Same as in panels **a**–**b** but calculated for spikes in a −1.5 s to 1.5 s time window around stop signals (delta-coupled units, $n = 34$; successful and failed stop attempts, $n = 30$ each). Circular uniformity was tested with Rayleigh's test (all stop trials, $p = 0.011$; successful stops, $p = 0.277$; failed stops, $p = 0.57$; two-sided test). Outliers are not shown for better visualization; see Supplementary Fig. S8 for all data. Source data are provided as a Source Data file.

confirming the importance of the time window around the go signal with respect to response inhibition.

Bursting STN neurons are less responsive to go signals, less predictive of inhibitory performance and a subset of them strongly lock to delta

Most STN units showed bursting activity (Fig. 7a), as expected based on previous literature[25,26]. We defined a burst index (BI) based on the presence of short-lag peaks (so called burst shoulders) in the spike autocorrelogram of units (see Methods[27]) and binarized units as bursting or non-bursting using an empirical BI threshold of 0.35 based on previous studies[28,29]. This resulted in 105 bursting (70%) and 45 non-bursting units (30%) out of 150 units with >1000 spikes. Average autocorrelograms confirmed the presence and absence of burst shoulders in bursting and non-bursting units, respectively (Fig. 7b).

In line with previous studies, bursting was stronger towards the dorsal part of STN and closer to the centroid of the motor subregion[30] (Supplementary Fig. S10a–c). Postoperative UPDRS scores (DBS stimulator turned on) showed a significant positive correlation with the BI of the recorded units (Fig. 7c, Supplementary Fig. S7h). Moreover, postoperative UPDRS scores correlated better with STN bursting than preoperative UPDRS scores (Supplementary Fig. S10d), which may indicate that motor symptoms in DBS-implanted patients have a strong connection with STN function. We did not find any significant correlations between median RT or SSDp05 and BI (Supplementary Fig. S10e).

Next, we asked whether STN units responsive to go signals differed in their activities depending on their burstiness. By performing a median split of STN units based on BI, we found that strongly and weakly bursting go-activated STN neurons showed comparable responses to the go signals. When we compared successful and failed stop trials, stronger go-elicited activation was associated with failed stops in both groups (Fig. 7d, Supplementary Fig. S7j), similar to what we found when all units were considered (see Fig. 4b). Nevertheless, the difference was larger and appeared earlier for weakly bursting units.

We performed the same analysis for units that were inhibited following the go signals. Here, we found that weakly bursting neurons were characterized by significantly larger inhibitory responses than strongly bursting units. These weakly bursting units also showed larger go signal-associated inhibition in failed vs. successful trials (Fig. 7e, Supplementary Fig. S7k). Thus, strongly bursting units were both less responsive and less predictive of inhibitory control performance, likely representing a Parkinson-related STN dysfunction.

Strongly bursting units coupled to a significantly later phase of STN LFP delta activity (mean angle, 2.44 (139.8°) for high BI and 0.77 (44.1°) for low BI; $p < 0.05$ two-samples Watson's test of homogeneity, Supplementary Fig. S10f, S7i), with similar phase coupling strength as weakly bursting units (Supplementary Fig. S10f), when examining phase-coupling around go signal presentation (but not around stop signals, Supplementary Fig. S10g). When only the single unit activities were considered without including multiunits, strongly bursting neurons showed significantly higher delta-coupling strength than weakly bursting neurons (Supplementary Fig. S7i), indicating that stronger delta PC might be characteristic to bursting units. When we focused on go-inhibited neurons where the largest difference between weakly and strongly bursting neurons was seen (Fig. 7e), we again found stronger delta PC in strongly bursting neurons as well as a positive correlation between BI and PC strength measured by MRL (Fig. 7g, Supplementary Fig. S10i). Since stronger delta phase locking was associated with unsuccessful response inhibition (Fig. 5e and j), it is conceivable that the disease-related dominance of bursting STN units in patients with PD impairs inhibitory control.

STN activity at the recording site predicts the direction of RT change after DBS surgery

Although we did not find population level differences in SSRT performance related to DBS surgery or DBS stimulation (Fig. 1), patients were categorized by either an increase or a decrease in RT following DBS surgery (DBS-on) compared to preoperative reaction times (Fig. 8a). As expected, SSDp0.5 estimations showed changes mostly concordant with median RT (Fig. 8b–c; Supplementary Fig. S11). Since average stop performance also changed in the direction of median RT, a better preoperative stop performance turned into worse performance postoperatively in the RT decrease group (Fig. 8d), in agreement with a possible decrease in decision thresholds[19,31].

About half of the patients showed a postoperative decrease of RTs, whereas other patients showed a postoperative RT increase. UPDRS scores, year of disease onset, disease duration, indices of postoperative motor improvement and levodopa equivalent daily dose (LEDD) reduction were assessed, but none of these explained the difference (Supplementary Fig. S12a-c).

We tested whether STN activity was predictive of this outcome of the interventions. Interestingly, we found that STN units recorded

https://doi.org/10.1038/s41467-026-71502-z

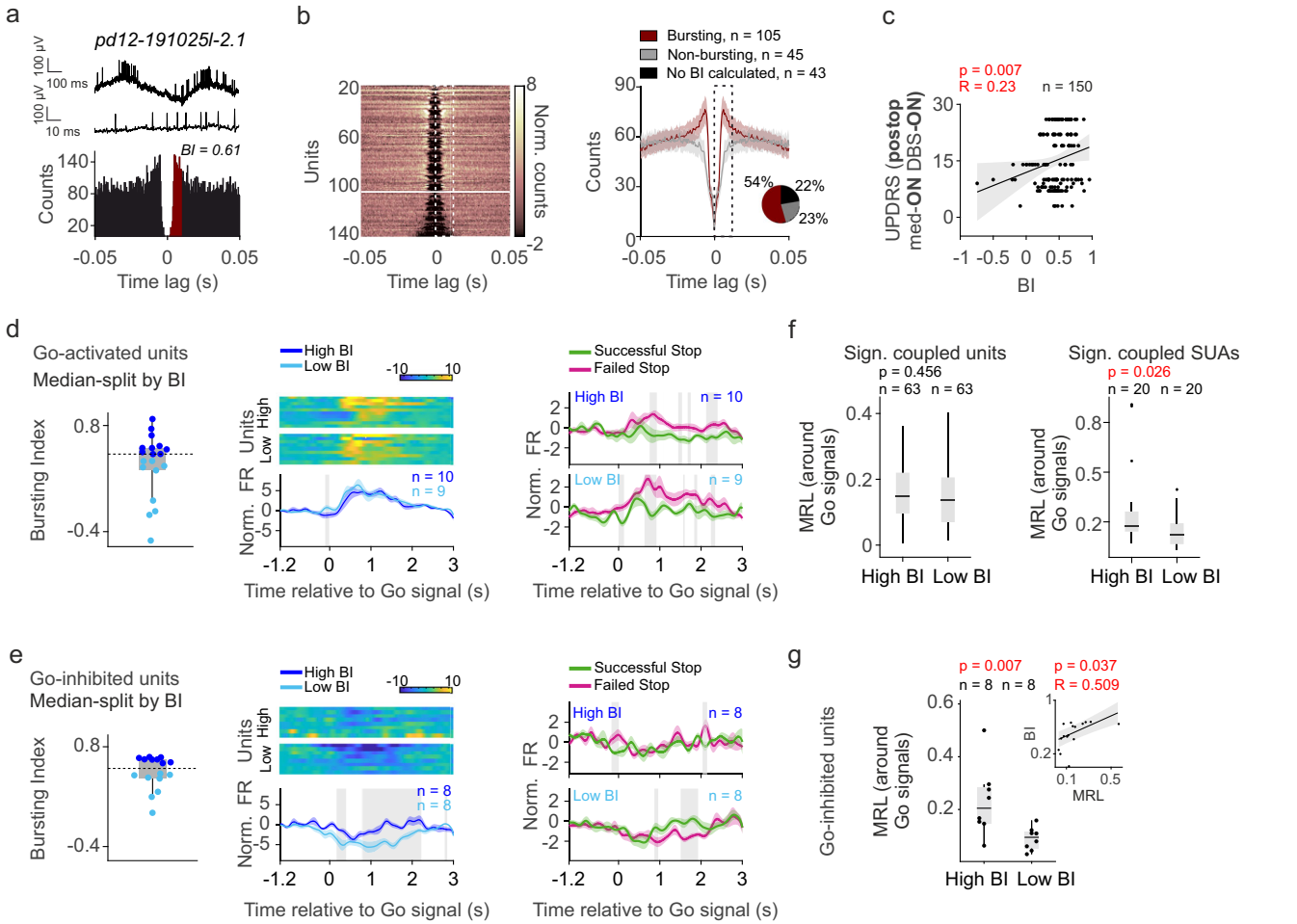

Fig. 7 | Bursting STN neurons are less responsive to cues, less predictive of inhibitory performance and a subset of them strongly lock to delta. a Top, bursting unit (raw trace). Bottom, spike autocorrelogram (AC) showing burst shoulders. The time lags used for calculating the bursting index (BI) are highlighted. **b** Left, ACs of all recorded units with >1000 spikes (bursting units above horizontal line). Right, average AC of bursting (brown, $n = 105$) and non-bursting (gray, $n = 45$) units (shading, SE; dashed boxes, time lags used for BI calculation). Inset, proportion of bursting and non-bursting units. **c** Correlation between BI and postoperative UPDRS scores (medication on, DBS on) across units ($n = 150$). Line, robust regression; shading, 95% CI. Pearson's r and corresponding p-values (two-sided t-test) are shown. **d** Go-activated units split by median BI. Left, box-whisker plot of BI distribution (median, dashed line; interquartile range and non-outlier range). Middle, PETH for low BI ($n = 9$) and high BI ($n = 10$) units (yellow, activation; blue, inhibition) and PETH averages (shading, SE). Right, average PETH of successful (green) and failed (pink) stops within each BI group. Gray, significant differences ($p < 0.05$, two-sided permutation test with cluster-based correction). **e** Same as in panel **d** for go-inhibited units (low BI, $n = 8$; high BI, $n = 8$). Box-whisker plot: median, interquartile and non-outlier ranges. **f** Delta coupling strength around go signals (−1.5 to 1.5 s) in units split by median BI. Left, significantly delta-coupled single- and multi-units (high BI, $n = 63$; low BI, $n = 63$). Right, single-units only (high BI, $n = 20$; low BI, $n = 20$). Box-whisker plot: median, interquartile and non-outlier ranges. Two-sided Mann−Whitney U-tests. **g** Go-inhibited units split by median BI. Delta coupling strength of low ($n = 8$) and high BI ($n = 8$) units differed significantly ($p = 0.007$, two-sided Mann-Whitney U-test). Inset, correlation between MRL around go signals and BI, with robust regression (shading, 95% CI) and Pearson's r (two-sided t-test). Box-whisker plot shows median, interquartile range and non-outlier range. Source data are provided as a Source Data file.

from patients with RT increase showed higher burst index (Fig. 8e). It is conceivable that small differences in electrode positioning could underlie this effect, that is, targeting a region with more bursting neurons more likely led to an increase of RT. However, when we carried out a systematic analysis of potential correlations of stimulating electrode positioning and postoperative reaction times, we only found relatively weak evidence for this (Supplementary Fig. S12g-j).

We also found that STN units recorded from patients with RT increase showed larger activation after go signals (Fig. 8f), which was associated with failed stop attempts when all responsive units were considered (see Fig. 4b). STN neurons inhibited around go signals showed weaker inhibition in patients with postoperative RT increase (Fig. 8f), a possible consequence of stronger bursting activity that was associated with smaller responses in this group of units (see Fig. 7e; no difference in the response magnitude of stop-responsive units were found, Supplementary Fig. S13a–b).

The number of delta-coupled units (Supplementary Fig. S13c) and the mean phase of coupling around go and stop signals were similar in the two patient groups (Watson's two sample test of homogeneity, $p > 0.05$; Supplementary Fig. S13d–e). Interestingly, STN units in patients with RT increase were less coupled to delta activity around go signals (Fig. 8g), but more strongly coupled around stop signals (Fig. 8h). The latter difference was larger, which might suggest a stronger local STN impairment in patients with postoperative RT increase, based on the association of stronger delta coupling with failed stop attempts (see Fig. 5e, j).

Discussion

Stop signal reaction time task before, during and after DBS implantation surgery

We have examined the SSRT performance of 13 patients with PD prior to, during and following DBS implantation surgery. We have not

https://doi.org/10.1038/s41467-026-71502-z

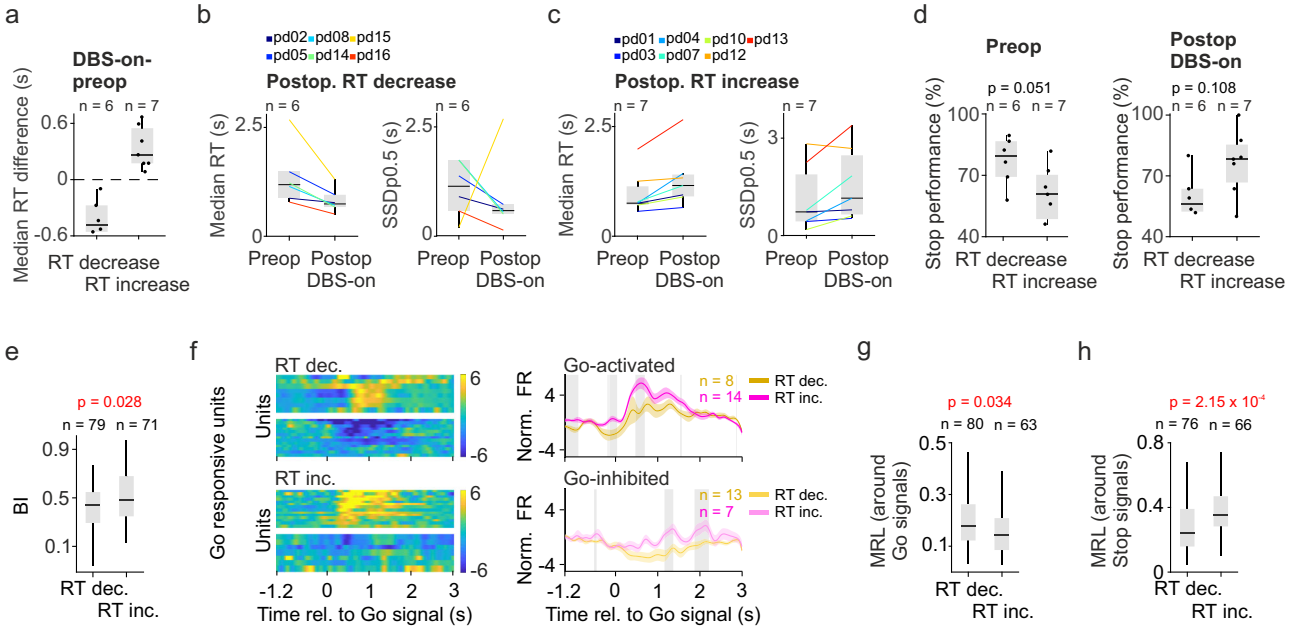

Fig. 8 | STN activity at the recording site predicts the direction of RT change after DBS surgery. a–d Patients were grouped by the direction of RT change when comparing postoperative DBS-on to preoperative condition (left side sessions). Box-whisker plots show median, interquartile range, and non-outlier range. **a** Magnitude of RT change of patients with RT decrease ($n = 6$) and RT increase ($n = 7$; left side). Outliers are not shown for better visualization; see Supplementary Fig. S11i-j for all data. **b** RT (left) and SSDp0.5 (right) of patients with RT decrease ($n = 6$). **c** RT (left) and SSDp0.5 (right) of patients with RT increase ($n = 7$). Each line corresponds to one patient. **d** Stop performance in patients with RT decrease ($n = 6$) and RT increase ($n = 7$), in preoperative (left) and postoperative, DBS-on sessions (right). See Supplementary Fig. S11g-h for plots including outliers. **e** Comparison of BI of STN units recorded from patients with RT decrease (RT dec., $n = 79$) and RT increase (RT inc., $n = 71$; $p = 0.028$, two-sided Mann–Whitney *U*-test). Box-whisker plots: median, interquartile and non-outlier ranges; see Supplementary Fig. S12d for plots with outliers. **f** Left, PETH of go-responsive units (yellow, activation; blue, inhibition). Right, mean PETHs (shading, SE). Gray shading, significant differences between PETHs of units from patients with RT decrease (go-activated, $n = 8$; go-inhibited, $n = 13$) vs. increase (go-activated, $n = 14$, go-inhibited, $n = 7$; $p < 0.05$, two-sided permutation test with cluster-based correction). **g** Comparison of delta coupling strength of STN units recorded from patients with RT decrease ($n = 80$) vs. RT increase ($n = 63$), spikes in −1.5 s to 1.5 s time window around go signals were included; shading, SE; two-sided Mann–Whitney *U*-test). Box-whisker plots: median, interquartile and non-outlier ranges; see Supplementary Fig. S13d-e for plots with outliers. **h** Same as in panel **g** but calculated for spikes in a −1.5 s to 1.5 s time window around stop signals (RT decrease, $n = 76$; RT increase, $n = 66$). Source data are provided as a Source Data file.

observed consistent changes in behavioral measures on a population level; however, there were significant changes on the level of individual patients: RT either increased or decreased following surgery compared to preoperative tests.

Numerous conflicting findings were reported on the effect of STN DBS on response control. While some researchers found unchanged RT with improved SSRT in response to stimulation[32,33], others described faster RTs along with unaffected[34], prolonged[35,36] or even improved SSRT[37]. A possible reason underlying these inconsistencies is that the STN is involved in distinct processes of inhibitory control. On one hand, it provokes an abrupt movement suppression (reactive stopping)[38], triggered either by a stop signal, canceling the already initiated response or by a conflict-inducing stimulus, calling for prolonged evidence accumulation[38]. In accordance, lesion studies of the STN showed impaired ability to inhibit initiated responses[39]. On the other hand, STN was suggested to control the tonic restraint (proactive inhibition) maintained to prevent premature responses[40]. Proactive inhibition presumes increased decision bound in face of conflicting situations in a strategic manner, preceding stimulus presentation. Greater RT difference between low- and high-conflict trials observed during stimulation[36] suggested a beneficial effect of STN DBS treatment on the control of proactive inhibition. Similar conclusions were drawn by manipulating bilateral STN DBS in a countermanding task[40]. Additionally, despite the increase in impulsive errors produced by STN stimulation[19,38,41], it simultaneously enhanced top-down suppression of conflict-induced interference effects[42]. Therefore, while decision thresholds are thought to decrease during STN DBS therapy, the better top-down control of proactive inhibition might partially counteract this effect resulting in reduced, but more dynamic threshold adjustments. Unilateral DBS applications in some studies may show limited effectiveness compared to bilateral implants, representing an added layer of variance across studies[43].

Reaction times might also be influenced by impaired motor execution, which may be reflected by the generally positive correlations between UPDRS scores and reaction times. In this regard, shorter RT's might not only reflect impulsive decisions but also improved motor execution[44]. An analysis of performance did not resolve this question due to low error rates and variability in behavior. Additionally, STN may also modulate non-motor functions, such as discriminative attention[45] or regulation of emotional relevance[46,47], which further complicates the interpretation of stimulation effects. However, altogether, the group of patients demonstrating slower RT following DBS implantation might have improved in proactively inhibiting their movements[38]. Importantly, the changes in RTs were concordant between DBS-off and DBS-on conditions, indicating a long-term stimulation effect. In contrast with the prompt diminution of motor symptoms in response to stimulation, cognitive effects may emerge more gradually over the long-term treatment.

Frontal and STN delta power increased during SSRT performance

We found increased delta band activity around go signals both in the frontal cortex and in the STN[12], and stronger STN and frontal delta power around go signals was associated with faster patient reactions,

as also shown before[7,48,49]. RT is influenced by multiple concomitant control mechanisms: processing of the go cue, response initiation and execution that facilitate, as well as proactive inhibition that actively slows responses, making it challenging to differentiate the exact source of faster RTs. In the frontal cortex, delta activity continued to increase after stop cues, whereas the STN showed a concurrent decrease. These suggest that STN delta may be more related to go signal processing, movement execution or movement preparation, while frontal delta rather correlates with conflict anticipation[6,7] and inhibitory control[12]. Consistent with this, albeit frontal-STN delta band coherence decreased during the go signal, maintaining a relatively higher coherence was a prerequisite of successful stopping. These observations support the notion that delta band processes of different sources may be superimposed in the STN.

Failed stop attempts were associated with lower fronto-central delta power that could be a sign of decreased top-down influence through the hyperdirect pathway[13] and were followed by an increase of frontal-STN delta band coherence, possibly indicating top-down control signals arriving late[2]. Additionally, the negative correlation between delta amplitude in fronto-central regions and RT (Supplementary Fig. S4g) indicates that the delta difference in successful and failed stop trials cannot be explained by the delta amplitude - RT correlation. This also supports that larger delta associated with successful stops is related to inhibitory processes.

When comparing EEG recordings with DBS stimulation off and on, we found that the frontal delta band power increase related to go signal presentation was smaller in magnitude and shorter in duration with DBS turned on. This is consistent with a reduction in inhibitory control during STN stimulation, as earlier reports proposed[20,50]. Higher frontal delta band activity before stop signals were associated with successful response inhibition both DBS on and off, emphasizing the role of the hyperdirect pathway during a brief time window around the stop signal in inhibitory motor control[51].

Cavanagh et al. proposed that slow frequency bands may reflect a neural substrate for cortico-basal ganglia communication regulating decision processes[12], whereas in another study Tan and Brown found that force and movement vigor were rather represented by higher frequency bands in the STN[52]. Our results largely confirm this; however, we found that STN delta band activity around the go signals may partly represent go stimulus processing and/or response preparation, also confirmed by the association of larger STN delta power increase with faster patient responses to go signals. Concomitantly, lower frontal-STN delta coherence was also associated with faster RTs, further supporting the inhibitory role of STN-frontal synchronization in the delta band. These observations are supported by previous reports linking faster RTs to larger STN power and lower frontocentral-STN phase-locking in the low frequency range[53]. This makes the STN an integration site of go and stop processing, resonating with the race model of action cancelation proposed by Schmidt and Berke[2], but suggesting that integration not only happens in the substantia nigra pars reticulata, but already upstream in the STN, consistent with the STN being a key hub for decision making under conflict[54].

Given the prominence of beta band activity in Parkinson's disease[55] and its role in movement suppression[56,57], we also assessed beta-band activity changes, while our main focus remained the less investigated delta frequency band. We observed a broad decrease in beta power following the go signal, corresponding to the centro-parietal beta desynchronization described in several studies[58,59]. We also found that beta increased following the stop signal, mainly in the fronto-central region and that successful stops were associated with higher right frontal beta. This is consistent with previous evidence on beta power increase in the right inferior frontal cortex associated with successful action cancellation[60]. Therefore, the beta band shows opposite effects compared to delta activity during movement execution, however, successful stopping is associated with both increased delta and beta power. Importantly, delta increase associated with successful stopping appears earlier, before the stop signal, while increased beta emerges right after the stop signal. This suggests that beta is associated with fast inhibitory control, while delta may be more related to proactive inhibition processes.

Increased go signal-related activity and local delta band synchrony in the STN impairs inhibitory control

Although a number of studies investigated STN LFP and also delta band activity in particular, as discussed above, few animal[2,61] and even scarcer human studies[62] investigated the neuronal activity in the STN with respect to inhibitory motor control[13–15,63,64] or decision making under conflict[65–67]. Therefore, the relation of human STN spiking with local delta band activity remained unclear. We found that about half of the STN units exhibited diverse responses to behaviorally relevant events including go signals[61], stop signals[2,14] and key press movements[14], demonstrating an active engagement of the STN during SSRT performance, in line with previous animal and human recordings.

Consistent with the finding that STN delta band activity might at least in part reflect go instruction processing, failed attempts to stop were associated with increased go-signal-evoked activation in the STN, potentially indicating more advanced cue processing hindering the ability to stop. This is supported by reports on the valence specificity of STN neurons responsive to both go and no-go stimuli[63]. In line with this, a subset of neurons differentiated successful from failed stop attempts by differential firing rates before stop signals, thereby predicting inhibition outcome. While some animal[2] and human studies[14] found fast stop-signal-elicited responses in STN neurons emphasizing its role in reactive stopping, the presence of outcome predictive STN units in comparable proportions supports the notion of STN being also involved in proactive inhibition[68]. Combining this with former reports[14,69], it is conceivable that the ventromedial STN is more associated with reactive stopping, while proactive inhibition is localized more to the dorsolateral part. A larger sample of unequivocally localized STN units will be required to determine this in the future.

We found that local STN delta power and unit activity were not independent: a large fraction of STN units showed phase coupling in the delta frequency band with most units preferably locked to the rising phase of delta. If significant delta phase coupling reflected coupling to an event-related potential evoked by go- or stop signals, phase-coupled units would have exhibited a consistent temporal alignment relative to these behavioral events, i.e., they would have been identified as responsive units. However, we identified far more delta-coupled units than responsive units, while not all responsive units demonstrated significant delta phase coupling. Furthermore, go-activated and -inhibited delta-coupled units showed a significant phase preference to the ascending phase of delta, whereas if both activated and inhibited units were coupled to an event-related potential, they would have been coupled to different phases of the underlying potential. Although an unequivocal disambiguation may be challenging, the above notions argue for phase- rather than time-aligned STN activities (Supplementary Fig. S8j–l). Evaluating the temporal dynamics of delta phase coupling is challenging, especially during a behavioral task with multiple events in rapid succession. The assessment of delta-related coupling requires the inclusion of at least one, but preferably more than one full cycle of the oscillation for each trial, presuming a time window of at least 2 s. Our approach was to convey a more reliable estimate of delta phase coupling at the expense of temporal precision, thus we defined 3 second time windows around salient events (go and stop signals). Nevertheless, a re-analysis in 2 second time windows before and after these events showed very similar results (Supplementary Fig. S9).

Somewhat unexpectedly, stronger phase locking predicted slower patient responses to go signals, suggesting that a strong delta phase coupling was not beneficial to go instruction processing.

Alternatively, slower RTs might have reflected, at least in part, proactively inhibited responses. In line with this, a subset of STN units were reported to couple more strongly to low frequency oscillations (2–8 Hz) during high conflict trials, with similar phase preference as observed in our data[66]. However, despite longer reaction times, stronger phase locking was also associated with failed stop attempts. This association was particularly apparent for STN units that were inhibited upon go signals, suggesting that this group might be of special relevance in response inhibition. Although the presence of such neurons was reported in monkeys (Fig. 3 in ref. 61), their roles in neuronal processing and control of behavior have not yet been investigated. The special role of go-inhibited units in cognition was also highlighted by a study on speech production, where STN units demonstrating decreased firing rate were linked to cognitive aspects of speech, while those producing increased firing rate were associated with motor aspects[70]. Thus, increased local delta band synchrony, indexed by stronger phase coupling of STN units to local delta band activity, might impair reactive inhibitory motor control. This supports the hypothesis that the ability to release proactive inhibitory control is impaired in PD patients[68], hampering both movement initiation and switching to reactive stopping. To further test this, we compared trials with a 3-1 stimulus sequence, presumably of high conflict due to the inverted order and the skipped button, with low conflict 1-2 sequence stimuli. While we could not detect significant difference in frontal EEG or STN LFP delta power, high conflict trials were associated with lower delta PC strength in those patients where 3-1 stimuli were associated with slower RTs, in accordance with lower delta PC observed in successful stop trials (Supplementary Fig. S8g).

Bursting activity of STN neurons was found to be increased in PD; therefore, it is often considered part of the pathophysiology[17,18]. However, we note that based on data from healthy primates, burst firing occurs in STN units under physiologic conditions due to their intrinsic membrane properties[26,71], triggered by hyperpolarization of STN units[72]. Patients with essential tremor also showed STN bursting in a smaller fraction of cells, suggesting that PD only enhances bursting activity that may normally also be present[18]. Our estimates of the proportions of bursting STN units in PD patients matched former reports[18].

The STN may be affected by PD pathology in a spatially inhomogeneous manner, and thus burstiness measured on a single recording site does not necessarily correlate with the clinical pathology that likely arises from multiple sources. Also, recording was not necessarily at the final position of the DBS stimulation contact sites. Still, STN bursting exhibited a significant positive correlation with the postoperative UPDRS score with DBS turned on, suggesting that the presence of many strongly bursting STN units at the recording site predicted worse postoperative motor outcome. This association of bursting with postoperative UPDRS evaluation surpassed that of with preoperative UPDRS scores, suggesting that clinical symptoms in DBS-implanted patients have a strong connection with STN function.

STN units inhibited upon go signals with less bursting showed larger inhibition, especially in failed stop trials. This mirrors the larger activation of go-signal-activated units in failed stop attempts, raising the possibility that inhibitory connections shape the activity of these neuronal groups[73]. In the same group of go-inhibited units, more bursting was associated with stronger delta phase locking, which we found detrimental to SSRT behavior (see above). This was further substantiated by a significant positive correlation between bursting strength and delta band phase locking. Altogether, stronger bursting was linked to weakened responsiveness, stronger delta phase locking and less predictive power with respect to movement cancellation performance, suggesting that the dominance of the bursting STN phenotype in patients with PD impairs inhibitory motor control.

Interestingly, most of the differences between successful and failed stops observed in our study were found before the stop signal. Successful stops were associated with higher frontal delta, stronger frontal-STN coherence, decreased firing of go-activated units and weaker suppression of low-bursting go-inhibited units. These findings indicate either weakened pro-kinetic or strengthened proactive inhibitory processes. Reactive control was shown to be impaired earlier in PD patients than proactive control[74], while impaired proactive control was shown to result in the difficulty of releasing the inhibition[68]. Therefore, proactive inhibitory processes might be important contributors to response control mechanisms in patients with PD. However, lower number of stop than no-stop trials may have also contributed to detecting less differences between successful and failed stops around the stop signals.

Stronger burst firing activity at the implantation site predicted a postoperative increase of reaction times

The sampled STN region of patients characterized by increased RT following STN implantation showed higher bursting index of STN units, which might be related to PD pathology, as discussed above. Bursting especially affected the activity of go-inhibited units in this patient group, which showed diminished responsiveness. At the same time, increased responsiveness of go-activated units, associated with unsuccessful stops, might reflect impaired inhibitory control. Larger go-activation due to better preserved movement initiation was not likely, since the preoperative RT of patients with postoperative RT increase and RT decrease was comparable.

In line with this, there is evidence that patients with STN neurons with higher intra-burst frequency were less prone to develop impulsive-compulsive behaviors following STN DBS implantation, regardless of motor symptoms[75]. Another study found that stopping functions might be altered in opposite directions depending on baseline performance: stimulation improved response inhibition in patients with slower baseline SSRT compared to control subjects, while impaired stopping in those with baseline scores matching the control group[34]. This supports the idea that increased RT observed in our data is associated with better control of proactive inhibition.

Since bursting index correlated positively with delta PC strength, greater coupling would be expected in patients with RT increase, which was found around stop signals but not around go signals. Nevertheless, the delta phase locking difference was larger in association with the stop cues, suggesting stronger local delta synchrony of STN units in patients with RT increase. Provided that stronger STN delta phase locking correlated with failed stop attempts, this may also indicate the STN's involvement in impaired decision making in the patient group where the implantation surgery led to slowed behavioral responses.

It remains open whether the differential STN activity patterns we observed that predicted the effects of DBS on RTs reflected a general difference across patients with respect to their STN dysfunction, differential STN firing patterns at the recorded area influenced by differential electrode positioning, or a combination of both. In support for the role of the position of the stimulated contact, we found that patients with faster RTs were stimulated closer to the limbic centroid of the right STN. This would imply that with carefully chosen locations for stimulation, a better outcome on impulsive decisions could be achieved; however, further specific tests of this hypothesis will be required. Nonetheless, this notion is supported by former studies, which found that stimulation of ventral STN caused inhibitory deficit[76], while stimulation of dorsal STN improved inhibitory functions[77]. While early implantation was shown to result in motor improvements comparable to later stage surgeries[78,79], local STN pathology has not been assessed in these studies.

Methods

Patient selection

Thirteen patients with Parkinson-disease (6 males; age, 60.92 ± 12.6 years; Supplementary Table S1) undergoing bilateral STN DBS

implantation (Supplementary Table S2) were enrolled in this study, recruited from the Institute of Neurosurgery and Neurointervention (formerly National Institute of Clinical Neuroscience) of Semmelweis University (Budapest, Hungary). Informed consent was obtained from all subjects. Informed consent forms and all research protocols were approved by the Institutional Research Ethics Committee of NIMNN or its predecessors (OKITI IKEB1/2018; OMIII IKEB 21/2023) and the National Scientific and Ethical Committee of the Medical Research Council, Budapest, Hungary (OGYÉI/64814-6/2023). Subjects were not compensated for their participation. All research methods were performed in accordance with the relevant guidelines and regulations (Clinical Trials Directive (EC) No. 2001/20/EC, Note for Guidance on Good Clinical Practice (CPMP/ICH/135/95), the Declaration of Helsinki, Codex of Bioethics (2nd edition, Medical Research Council, Hungary), and Hungarian regulations Act CLIV of 1997 on Health; Act C of 2012 on the Criminal Code Chapter XVI; decree 33/2009. (X. 20.) of the Minister of Health on the clinical examination of medical devices; decree 23/2002. (V. 9.) of the Minister of Health on medical research involving humans).

Clinical evaluation

Motor symptoms (UPDRS-III) of patients were evaluated at baseline and at the time of postoperative testing, both in off-medication state following 12-h withdrawal of anti-parkinsonian treatment and in on-medication condition. Postoperative evaluation was performed with STN DBS stimulation turned on. Improvement in motor functions following implantation was quantified by calculating the difference between preoperative and postoperative UPDRS scores (off-medication), divided by the postoperative scores (off-medication)[80].

Stop signal reaction time task paradigm and behavioral analysis

The apparatus for the behavioral task consisted of 1. a custom-designed, 3D-printed ergonomic button box, featuring three buttons and containing an Arduino board (Arduino Leonardo, Arduino SRL), which detected and timestamped button presses and screen presentations; 2. a screen (size, 15.6 inches; resolution, 1366 × 768; refresh rate, 60 Hz) displaying the go signal, the stop signal and feedback; 3. a photo-sensor mounted on the upper left corner of the screen that was connected to the Arduino board to log exact times of screen presentations; 4. a notebook running custom-written, Psychtoolbox-based[81] Matlab code that controlled running of the task; 5. a pulse train generator (Pulse Pal v2, Sanworks LLC[82]) sending TTL pulses to the data acquisition system, triggered by the output of the Arduino board, for precise synchronization of behavioral and brain data. In intraoperative recordings, the isolated TTL signal was connected to an active EMG channel of the data acquisition system; in postoperative recordings, TTL pulses were sent to a dedicated trigger channel of the EEG recording system.

We adapted the SSRT task to Parkinson's patients by choosing the go task to be difficult enough to obtain sufficiently long SSDs, but simple enough to be manageable for PD patients during surgery. Patients viewed visual stimuli on a screen displaying two integers between 1 and 3 presented simultaneously next to each other (go signal), and they were instructed to press the corresponding buttons in the same order as quickly as they can on a custom-designed button box (approved utility model U2200127; submitted patent application P2200356 and PCT/HU2023/050054). After patients responded by key presses, a feedback screen appeared stating whether the response was correct (over green background), or incorrect (over red background). In a subset of the trials, the screen featuring the go stimuli was followed by a STOP signal (over red background) presented at variable delays, instructing patients to withhold button pressing. The SSD was updated for each trial based on the past 5 reaction times. The percentage of stop trials from all presented trials within one session was 19.4 ± 7% (mean ± SD). If patients failed to withhold button pressing, a feedback screen over red background informed them about the unsuccessful stopping. In case patients managed to refrain from pressing during a 2 s response window, a feedback screen over green background reinforced the successful stop response. The task was performed first with the right, then with the left hand preoperatively (only right hand: pd01, pd02) and also during implantation (only right hand: pd01; only left hand: pd03). Postoperative measurements started after a 12-hours withdrawal of PD medication and at least 60 min after DBS was turned off. Patients performed the SSRT task first with their right, then with their left hand with 60-channel EEG and EMG monitoring (only left hand: pd05, pd16; no tests: pd07). Next, the DBS stimulator was turned on and after 10 minutes of pause, the task was repeated for the right hand (pd04, pd05, pd13, pd14, pd15, pd16), the left hand (pd10) or both hands (pd01, pd02, pd08, pd12).

RT was calculated as the time interval between cue presentation and the first key press. Median RT was calculated after excluding outliers (values exceeding three scaled median absolute deviations from the median). SSDp0.5 was computed after fitting a generalized linear regression model (binary logistic regression) with response variables as successful (1) and failed stop (0) trials and corresponding SSD values as explanatory variables (Fig. 1c). SSDp0.5 corresponded to the value of 0.5 probability. Task performance was calculated as the percentage of correct trials relative to the total number of go trials (i.e., trials without a stop signal presentation). Stop performance was defined as the percentage of successful stop trials relative to the total number of stop trials.

Neurosurgical procedure

Bilateral DBS leads (St. Jude Medical Infinity 6170 / Boston Scientific Vercise Cartesia 2202; Supplementary Table S2) and pulse generator (IPG) were implanted for each patient. For individual anatomical planning, preoperative MRI (contrast-enhanced 3D T1 weighted and T2 weighted images obtained with a 3 T Phillips Achieva MRI scanner no more than six months in advance of implantation) were merged with stereotactic CT scan acquired on the day of the surgery (contrast-enhanced CT with a Leksell G frame fixed on the patient's head). For preoperative planning, Medtronic StealthStation S7 Cranial software was employed. Standard stereotaxic principles were applied to select individual anatomical targets in the STN[83]. Trajectories were planned based on individual anatomical structures.

Dopaminergic medication was discontinued 12 h prior to the surgery. The implantation of the DBS leads was accomplished using local anesthetics, while the IPG was implanted under general anesthesia. The pre-planned trajectory was monitored with five microelectrodes (in anterior, lateral, medial, posterior and central positions), while one macroelectrode was used for delivering stimulation to assess the clinical outcome. The permanent DBS lead was implanted to the selected microelectrode trajectory. During gradual descent of the microelectrodes, the procedure was halted when the surgical team determined likely positioning in the STN with sufficient single unit quality (not necessarily at target depth).

Microelectrode localization

Localization of the microelectrodes were reconstructed post hoc by the fusion of postoperative contrast-enhanced CT (acquired six weeks after implantation) with the preoperative T1 MRI scans, using the Medtronic StealthStation S7 software. After manually reconstructing the trajectory of the implanted electrode based on the CT artefact, the trajectories of the other 4 microelectrodes were extrapolated from the intraoperative position, the dimensions of the Ben-Gun and the depth of the final electrode with respect to the planned target position.

Additionally, diffusion tensor imaging (DTI) was also performed and subregions of the STN were identified based on the connectivity profile of the STN. DICOM images were converted to compressed NIFTI format using MRICron's dcm2niix converter. Tools available in

the FMRIB Software Library (FSL 6.0.6.2) were used for linear and non-linear image registrations, and DTI data processing. Results of GPU based calculations have been obtained on a computer equipped with a Geforce Titan Xp, running Elementary OS 7. Probabilistic parcellation and anatomical classification of cortical surfaces according to the Destrieux Atlas was carried out using Freesurfer 7.3.2[84]. Classification targets for probabilistic tractography were created by combining cortical regions according to their designated functions, resulting in 3 target structures: limbic, motor, and sensory areas. The subthalamic nuclei, determined as seed regions, were manually delineated by two researchers independently on T2 images in mrview (MRtrix 3.0.4). DTI images were corrected for motion, eddy currents and EPI distortions using tools available in FSL 6.0.6.2[85].

B0 non-diffusion volumes were visually inspected to rule out any severe artifacts before further analysis. Estimation of diffusion tensors and crossing fibers was carried out according to methods described by Behrens et. al[86]. using the GPU-based implementation of BedpostX with the following parameters applied: burn in value: 1000, number of fibers per voxel: 2, fudge factor: 1, applied deconvolution model: zeppelin.

Probabilistic fiber tracking was carried out using GPU-based implementation of ProbtrackX[87] (FSL 6.0.6.2) with the following parameters applied: curvature threshold: 0.2, step length: 0.5, number of samples: 5000, volume fraction before subsidiary fiber orientations considered: 0.01, modified Euler streaming. The STN was selected as a seed region, while cortical areas described earlier were defined as classification targets for tractography in each hemisphere independently. The corpus callosum was selected as an exclusion mask to restrict fiber tracking only to the ipsilateral hemisphere. Transformation matrices between anatomical and diffusion spaces were prepared using Flirt with 6 degrees of freedom and mutual information selected as cost function. The NIFTI files containing the STN subregions (motor, limbic, associative) were loaded into Medtronic StealthStation S7 software and were assessed manually to determine whether the microelectrode measurement points reached each subregion. The center of gravities (CoGs, centroids) of the STN subregions were calculated with fslmaths (FSL 6.0.6.2) and 3D Euclidean distances were determined between the microelectrode contact coordinates and the CoGs of the STN subregions.

Limitations of microeletrode reconstruction. Microelectrode reconstructions were based on the standard intraoperative positioning of the Ben-Gun; however, we lacked intraoperative imaging to confirm the reconstructed trajectories. This limitation may introduce inaccuracies in the calculated 3D distances between the CoG of the STN subregions and the recording sites. Additionally, localization of postoperatively stimulated contacts was calculated as the inner center of the full ring; therefore, single segments of directional DBS electrodes could not be differentiated.

Electrophysiological data acquisition and preprocessing of LFP/EEG data

Intraoperative microelectrode recordings were performed with the clinical microelectrode recording system (ISIS Microelectrode Recording (MER) System, Innomed Medizintechnik GmbH, Emmendingen, Germany), with 20 kHz sampling frequency. Additionally, two EEG electrodes placed at positions corresponding to F3 and F4 of the 10–20 system were also recording brain activity (connected to the EMG headbox module of the same MER system), resulting in one bipolar EEG derivation (F4-F3).

Postoperative EEG was recorded with a standard 60-channel recording system and EEG cap (Brain Products Co., Munich, Germany), with 2048 Hz sampling rate. Electrodes were positioned according to the extended 10–20 system.

As a first step, electrophysiological data was synchronized with behavioral events, based on timestamps saved by the electrophysiological recording system and by the experimental setup, respectively. Time series were aligned, and behavioral timestamps were converted to the MER/EEG system's clock. Logged events (go and stop stimuli) were matched with the corresponding MER/EEG trigger using a 50 ms tolerance. This resulted in a few unmatched events due to broken or undetected TTL pulses, for which timestamps were linearly interpolated using the matched timestamps.

In case of postoperative recordings obtained during DBS stimulation, the stimulation artefacts were removed using DBSfilt, an open-source Matlab toolbox developed for this purpose[88]. All data were resampled to 250 Hz and filtered using a 100 Hz low-pass filter (sinc FIR filter using a Hamming window with default parameters of the pop_eegfiltnew.m Matlab function of the EEGLab package[89]). Line noise was removed either by CleanLine filter[90] or by 45-55 Hz notch filter, if irregular noise escaped the CleanLine filter. Next, the data was epoched according to the synchronized behavioral events to time windows of −2 to 2 s around each behaviorally relevant event (go signal, first key press, stop signal, feedback). Epoched data was revised visually and trials with high amplitude noise were rejected manually.

In case of postoperative scalp EEG recordings, artifact-rejected data were high-pass filtered above 2 Hz for Independent Component Analyses (ICA)[91], by implementing fastICA algorithm[92] (EEGLab plugin). ICA components associated with eye movements, faulty electrodes, stereotypic muscle artefacts and/or pulse artefacts were rejected. Rejected ICA components were removed from data filtered above 0.5 Hz, to regain low-frequency components[91]. Average baseline (−2 to −1 s) amplitude was subtracted from each data epoch. Following these steps, scalp current densities[93,94] were calculated by using FieldTrip Matlab toolbox[95] (ft_scalpcurrentdensity)[96], implementing the spherical spine method[97].

Data analysis of LFP/EEG data

All preprocessing and data analyses were performed using open-source and custom-written Matlab algorithms (MATLAB Version: 9.7.0 (R2019b), The MathWorks Inc.)[98]. Time-frequency decompositions were performed on concatenated and z-scored data epochs using Morlet wavelets (cycle number, 6[99]), employing the algorithm of Torrence and Compo[100]. Individual time-frequency epochs were normalized for each frequency component using the full length of the epoch[101]. Event-related spectrograms were visualized as power changes relative to baseline (−1 to −0.5 s). When comparing conditions, a common baseline across the compared conditions was applied.

When analyzing STN LFP, time-frequency measures were averaged across all microelectrode channels. The dominant frequency range within the delta band (1–4 Hz) was determined around go and stop signals (−2 to 2 s windows) separately for calculating spike-phase coupling. The frequency component with maximal power (Fr_{peak}) after averaging across time and epochs was determined. Dominant frequency range was defined as $Fr_{peak} \pm Fr_{peak} / 6$.

Magnitude-squared wavelet coherence (MSWC) was calculated between each microelectrode channel and the F4-F3 derivation using the built-in Matlab function wcoherence.m. Similarly to spectrograms, MSWC maps were also averaged across microelectrode channels.

Single- and multiunit activity analysis

Clustering of action potentials (Fig. 4b–e) was performed off-line on the 20 kHz sampled MER recordings, using the MClust 3.5 Matlab-based spike sorting toolbox (A.D. Redish, https://github.com/adredish/MClust-Spike-Sorting-Toolbox.git)[102]. First, the automated KlustaKwik[103] algorithm was run to create 2 to 7 clusters using amplitude (peak-to-valley), waveform energy and the first three principal component of the waveform (WavePC1-3) as features. Next, clusters were manually inspected and (i) accepted (sufficient waveform quality and low proportion of refractory period violations in the autocorrelograms), (ii) rejected (insufficient waveform quality due to low

amplitude, high variance or strong drift, or high proportion of refractory period violations in the autocorrelograms), (iii) merged (if the cross-correlogram and temporal evolution confirmed the identity of the units) or (iv) further split by running KlustaKwik on the selected cluster (if multiple distinct waveforms could be observed within the cluster). Waveform distributions of the resulting accepted clusters were inspected, and clearly identifiable cluster contaminations were removed. Isolation distance and L-ratio was calculated using WavePC1-3 and waveform energy as features, as suggested by Schmitzer-Torbert et al.[104] for comparability across studies[15,70,105,106]. Clusters with Isolation Distance > 15 and L-ratio <0.02 were considered single units; all other accepted clusters were considered multiunits (ratio of single unit activities, 48/193; with a less conservatiev L-ratio threshold of 0.15 using only waveform energy and WavePC1, 75/193).

Clustered units were examined in terms of their responsiveness to behavioral events, using the CellBase open-source Matlab toolbox[107] (https://github.com/hangyabalazs/CellBase.git). Peri-event time histograms aligned to task events (go signal, key press, stop signal and feedback) were calculated using the ultimate_psth.m function of CellBase[107] open-source Matlab toolbox (https://github.com/hangyabalazs/CellBase.git). Bin size was 1 ms, and smoothing was performed with a Gaussian kernel of 20 ms standard deviation and a total width of 120 ms. The activity in the baseline window (−2.5 to −1 s relative to go signal; −3 to −1.5 s relative to key press and stop; 1.5 to 3 s relative to feedback) was compared to a test window (0 to 1 s for all events, $p < 0.05$). First, local extremes were found and checked whether they surpassed (possible activation) or fell below (possible inhibition) mean baseline spiking probability. Then, a smaller window around the local extreme was defined, as the interval between the timepoints where the PETH crossed half-distances between the local extreme and baseline average, respectively. The spike count in the resulting activation/inhibition time interval was compared to a matching baseline time interval, selected with an identical method within the predefined baseline window, using Mann–Whitney *U*-test (one-sided, due to the asymmetric alternative hypothesis). Spiking activity corresponding to stop trials of different outcome was assessed by calculating PETHs derived from trials partitioned to failed and successful stop trials. Units were considered predictive of stopping outcome, if there was a significant difference in their firing rates between failed and successful stop trials before stop signal presentation. For this, multiple time windows before the stop cue was tested (−2 to 0 s, −1.5 to 0 s, −1 to 0 s, −0.5 to 0 s, Mann–Whitney *U*-test).

Coupling of spiking activity to LFP delta phase was also investigated. Spikes within the interval of −1.5 to 1.5 s around the go or the stop signal were selected and pooled from all respective epochs. LFP recorded on the same channel as the examined unit was band-pass filtered within the dominant delta frequency band (see above) and then Hilbert-transformed. The phase angles of the resulting analytic signal were extracted. Phase angles at timepoints closest to spike times were collected. The angle and the magnitude of the first trigonometric moment of this phase distribution defined the preferred phase and coupling strength (mean resultant vector length, MRL) of the examined unit, respectively. Preferred phases of units significantly coupled to LFP delta (Rayleigh's test for circular uniformity, $p < 0.05$) were pooled to form a population phase histogram. MRLs of these units characterized the degree of LFP delta coupling at the population level. Spike count was controlled when comparing delta phase coupling measures across conditions (failed versus successful stop trials). The spike number of the condition with the least spikes was determined for each unit. Corresponding numbers of spikes were selected randomly from the condition with more spikes.

Burstiness was estimated by the presence of a short-lag peak (0-10 ms) in the autocorrelograms (AC) of the units. It was quantified by a bursting index, calculated by subtracting the AC counts in a baseline latency window (876–1125 ms, chosen as to eliminate potential dependence on delta-rhythmic fluctuations of spiking) from the counts in the 0–10 ms period and dividing the difference with the larger of the two counts. Units were grouped into bursting and non-bursting groups based on an empirical threshold of 0.35[28,29,108]. Additionally, strongly bursting units were compared to weakly bursting units by a median split of the burst indices.

STN units were shown to be somatotopically organized, associated with movement of the contralateral body parts[109]. Thus, we expect a consistent relationship of unit firing with STN LFP and behavior in our recordings. Therefore, all analyses of STN unit responsiveness, bursting and delta phase-coupling included data derived from both left and right side tests.

Statistics

Behavioral parameters were compared with Kruskal–Wallis and post-hoc Tukey–Kramer tests. For comparison within patient groups, Mann–Whitney *U*-test was applied.

Correlations of various task-, clinical- and electrophysiological parameters were quantified using Pearson's correlation and tested with *t*-test. In case of correlating delta power with RT, within-subjects time-frequency correlation maps were obtained (correlation was calculated for each individual time-frequency datapoint within the selected epoch, for each subject). Within-subjects correlation maps were then averaged across patients.

Changes relative to baseline for time-frequency power coefficients, and wavelet coherence maps were tested using permutation statistics ($n = 1000$ iterations, $p < 0.05$) with false discovery rate (FDR) and cluster-based correction. As FDR correction does not account for the inherently high auto-correlation of event-related spectrograms, we implemented a cluster-based correction method by generating the significant cluster distribution under the null based on random data epochs. First, random 4 s epochs ($n = 100$) were selected from the continuous (non-epoched) preprocessed data of each patient. Then, data was averaged across a smaller set of epochs ($n = 32$, corresponding to the median number of trials used for analyses, including all conditions) for each patient. Significant signal change relative to baseline was tested across subjects, applying the same method across data and control (permutation test with FDR correction, $p < 0.05$). Significant clusters were identified, for each canonical frequency band separately. The cluster with the largest cluster-level statistic (sum of *t*-values within a single cluster) was saved. Statistical testing across subjects using a set of 32 random epochs for each subject was repeated 200 times, resulting in a one-tail distribution of 200 cluster values. The 95th percentile was chosen as the threshold for cluster-based correction.

For time-frequency maps associated with successful/failed stop trials, permutation statistics with cluster-based correction was applied ($n = 1000$ iterations, $p < 0.05$), using Fieldtrip toolbox. Distribution of significant clusters was generated by permuting trial labels in 1000 iterations. Similarly, PETHs of successful/failed stop trials and low/high burst index units were also compared by permutation statistics with clustered-based correction ($n = 1000$, $p < 0.05$). Contrarily to time-frequency difference maps, PETHs are one dimensional, thus cluster correction is less robust against short peaks of noise. To reduce noise, we used a smoothing kernel of 0.08 on PETHs. Furthermore, we modified the method of cluster correction so that instead of clusters with the largest cluster-level statistic (sum of t-values within a single cluster), clusters with the maximal size were considered, as this approach is more robust to short high peaks and more sensitive to weaker but more widespread effects. Difference between average delta power of successful and failed stop trials (in selected time window and frequency range) was tested with Mann–Whitney *U*-test ($p < 0.05$).

Coupling of spikes to LFP delta was considered significant if the null hypothesis of uniform distribution of phase angles was rejected by Rayleigh's test for circular uniformity ($p < 0.05$). Circular distributions

of preferred phases were compared with two-samples Watson's test of homogeneity ($p < 0.05$).

Sex and/or gender were not considered in the study design. Sex was determined based on self-report. No analyses related to sex and/or gender were carried out due to sample size limitations inherent to human intraoperative electrophysiology studies.

Reporting summary

Further information on research design is available in the Nature Portfolio Reporting Summary linked to this article.

Data availability

Deidentified electrophysiological and behavioral data generated in this study have been deposited at https://figshare.com/articles/dataset/human-STN-delta_data/31359616 (https://doi.org/10.6084/m9.figshare.31359616.v2)[110]. Source data are provided with this paper.

Code availability

Unique code developed to analyze these data is available at https://github.com/hangyabalazs/human-STN-delta and https://zenodo.org/records/18679923 (https://doi.org/10.5281/zenodo.18679923)[111].

References

1. Jahfari, S. et al. Effective Connectivity Reveals Important Roles for Both the Hyperdirect (Fronto-Subthalamic) and the Indirect (Fronto-Striatal-Pallidal) Fronto-Basal Ganglia Pathways during Response Inhibition. *J. Neurosci.* **31**, 6891–6899 (2011).
2. Schmidt, R., Leventhal, D. K., Mallet, N., Chen, F. & Berke, J. D. Canceling actions involves a race between basal ganglia pathways. *Nat. Neurosci.* **16**, 1118–1124 (2013).
3. Bari, A. & Robbins, T. W. Inhibition and impulsivity: behavioral and neural basis of response control. *Prog. Neurobiol.* **108**, 44–79 (2013).
4. Herz, D. M. et al. Motivational tuning of fronto-subthalamic connectivity facilitates control of action impulses. *J. Neurosci.* **34**, 3210–3217 (2014).
5. Perugini, A., Ditterich, J. & Basso, M. A. Patients with Parkinson's disease show impaired use of priors in conditions of sensory uncertainty. *Curr. Biol.* **26**, 1902–1910 (2016).
6. Zhang, Q. et al. Low-frequency oscillations link frontal and parietal cortex with subthalamic nucleus in conflicts. *Neuroimage* **258**, 119389 (2022).
7. Chang, A., Ide, J. S., Li, H.-H., Chen, C.-C. & Li, C.-S. R. Proactive control: neural oscillatory correlates of conflict anticipation and response slowing. *eNeuro* **4**, ENEURO.0061-17.2017 (2017).
8. Nguyen, T. et al. Dynamical EEG indices of progressive motor inhibition and error-monitoring. *Brain Sci.* **11**, 478 (2021).
9. Khan, A. U. et al. Low-frequency oscillations in mid-rostral dorsolateral prefrontal cortex support response inhibition. *J. Neurosci.* **44**, e0122242024 (2024).
10. Ghahremani, A. et al. Event-related deep brain stimulation of the subthalamic nucleus affects conflict processing. *Ann. Neurol.* **84**, 515–526 (2018).
11. Zavala, B. A. et al. Midline frontal cortex low-frequency activity drives subthalamic nucleus oscillations during conflict. *J. Neurosci.* **34**, 7322–7333 (2014).
12. Cavanagh, J. F. et al. Subthalamic nucleus stimulation reverses mediofrontal influence over decision threshold. *Nat. Neurosci.* **14**, 1462–1467 (2011).
13. Chen, W. et al. Prefrontal-subthalamic hyperdirect pathway modulates movement inhibition in humans. *Neuron* **106**, 579–588.e3 (2020).
14. Mosher, C. P., Mamelak, A. N., Malekmohammadi, M., Pouratian, N. & Rutishauser, U. Distinct roles of dorsal and ventral subthalamic neurons in action selection and cancellation. *Neuron* **109**, 869–881.e6 (2021).
15. London, D. et al. Distinct population code for movement kinematics and changes of ongoing movements in human subthalamic nucleus. *Elife* **10**, e64893 (2021).
16. Rogers, K., Gold, J. & Ding, L. The subthalamic nucleus contributes causally to perceptual decision-making in monkeys. *bioRxiv Prepr. Serv. Biol.* https://doi.org/10.1101/2024.04.09.588715 (2024).
17. Lourens, M. A. J. et al. Functional neuronal activity and connectivity within the subthalamic nucleus in Parkinson's disease. *Clin. Neurophysiol.* **124**, 967–981 (2013).
18. Steigerwald, F. et al. Neuronal activity of the human subthalamic nucleus in the Parkinsonian and Nonparkinsonian state. *J. Neurophysiol.* **100**, 2515–2524 (2008).
19. Pagnier, G. J., Asaad, W. F. & Frank, M. J. Double dissociation of dopamine and subthalamic nucleus stimulation on effortful cost/benefit decision making. *Curr. Biol.* **34**, 655–660.e3 (2024).
20. Herz, D. M. et al. Mechanisms underlying decision-making as revealed by deep-brain stimulation in patients with Parkinson's disease. *Curr. Biol.* **28**, 1169–1178.e6 (2018).
21. Krack, P. et al. *Five-Year Follow-up of Bilateral Stimulation of the Subthalamic Nucleus in Advanced Parkinson's Disease From the Departments of Clinical and Bio-Logical Neurosciences (P. N Engl J Med* vol. 349 www.nejm.org (2003).
22. Verbruggen, F. & Logan, G. D. Automatic and controlled response inhibition: associative learning in the Go/No-Go and stop-signal paradigms. *J. Exp. Psychol. Gen.* **137**, 649–672 (2008).
23. Duque, J., Olivier, E. & Rushworth, M. Top–down inhibitory control exerted by the medial frontal cortex during action selection under conflict. *J. Cogn. Neurosci.* **25**, 1634–1648 (2013).
24. Senzai, Y., Fernandez-Ruiz, A. & Buzsáki, G. Layer-specific physiological features and interlaminar interactions in the primary visual cortex of the mouse. *Neuron* **101**, 500–513.e5 (2019).
25. Ammari, R., Bioulac, B., Garcia, L. & Hammond, C. The subthalamic nucleus becomes a generator of bursts in the dopamine-depleted state. Its high frequency stimulation dramatically weakens transmission to the globus pallidus. *Front Syst. Neurosci.* **5**, 43 (2011).
26. Tai, C. H. Subthalamic burst firing: a pathophysiological target in Parkinson's disease. *Neurosci. Biobehav. Rev.* **132**, 410–419 (2022).
27. Royer, S. et al. Control of timing, rate and bursts of hippocampal place cells by dendritic and somatic inhibition. *Nat. Neurosci.* **15**, 769–775 (2012).
28. Hegedüs, P., Heckenast, J. & Hangya, B. Differential recruitment of ventral pallidal e-types by behaviorally salient stimuli during Pavlovian conditioning. *iScience* **24**, 102377 (2021).
29. Laszlovszky, T. et al. Distinct synchronization, cortical coupling and behavioral function of two basal forebrain cholinergic neuron types. *Nat. Neurosci.* **23**, 992–1003 (2020).
30. Kaku, H. et al. Unsupervised clustering reveals spatially varying single neuronal firing patterns in the subthalamic nucleus of patients with Parkinson's disease. *Clin. Park Relat. Disord.* **3**, 100032 (2020).
31. Herz, D. M. Neuroscience: therapy modulates decision-making in Parkinson's disease. *Curr. Biol.* **34**, R148–R150 (2024).
32. Swann, N. et al. Deep brain stimulation of the subthalamic nucleus alters the cortical profile of response inhibition in the beta frequency band: a scalp EEG study in parkinson's disease. *J. Neurosci.* **31**, 5721–5729 (2011).
33. Mirabella, G. et al. Deep brain stimulation of subthalamic nuclei affects arm response inhibition in Parkinson's patients. *Cereb. Cortex* **22**, 1124–1132 (2012).
34. Ray, N. J. et al. The role of the subthalamic nucleus in response inhibition: evidence from deep brain stimulation for Parkinson's disease. *Neuropsychologia* **47**, 2828–2834 (2009).

35. van den Wildenberg, W. P. M. et al. Deep-brain stimulation of the subthalamic nucleus improves overriding motor actions in Parkinson's disease. *Behav. Brain Res.* **402**, 113124 (2021).
36. Obeso, I., Wilkinson, L., Rodríguez-Oroz, M. C., Obeso, J. A. & Jahanshahi, M. Bilateral stimulation of the subthalamic nucleus has differential effects on reactive and proactive inhibition and conflict-induced slowing in Parkinson's disease. *Exp. Brain Res.* **226**, 451–462 (2013).
37. van den Wildenberg, W. P. M. et al. Stimulation of the subthalamic region facilitates the selection and inhibition of motor responses in Parkinson's disease. *J. Cogn. Neurosci.* **18**, 626–636 (2006).
38. Ballanger, B. et al. Stimulation of the subthalamic nucleus and impulsivity: release your horses. *Ann. Neurol.* **66**, 817–824 (2009).
39. Eagle, D. M. et al. Stop-signal reaction-time task performance: Role of prefrontal cortex and subthalamic nucleus. *Cereb. Cortex* **18**, 178–188 (2008).
40. Mirabella, G. et al. Stimulation of subthalamic nuclei restores a near normal planning strategy in Parkinson's patients. *PLoS One* **8**, e62793 (2013).
41. Frank, M. J., Samanta, J., Moustafa, A. A. & Sherman, S. J. Hold your horses: impulsivity, deep brain stimulation, and medication in Parkinsonism. *Science (1979)* **318**, 1309–1312 (2007).
42. Wylie, S. A. et al. Subthalamic nucleus stimulation influences expression and suppression of impulsive behaviour in Parkinson's disease. *Brain* **133**, 3611–3624 (2010).
43. Mancini, C. et al. Unilateral stimulation of subthalamic nucleus does not affect inhibitory control. *Front. Neurol.* **9**, 1149 (2019).
44. Hallett, M. Clinical neurophysiology of akinesia. *Rev. Neurol. (Paris)* **146**, 585–590 (1990).
45. Baunez, C. & Robbins, T. W. Bilateral lesions of the subthalamic nucleus induce multiple deficits in an attentional task in rats. *Eur. J. Neurosci.* **9**, 2086–2099 (1997).
46. Uslaner, J. M. & Robinson, T. E. Subthalamic nucleus lesions increase impulsive action and decrease impulsive choice - Mediation by enhanced incentive motivation? *Eur. J. Neurosci.* **24**, 2345–2354 (2006).
47. Serranová, T. et al. Subthalamic nucleus stimulation affects incentive salience attribution in Parkinson's disease. *Mov. Disord.* **26**, 2260–2266 (2011).
48. Cohen, M. X. & van Gaal, S. Subthreshold muscle twitches dissociate oscillatory neural signatures of conflicts from errors. *Neuroimage* **86**, 503–513 (2014).
49. Lavallee, C. F., Meemken, M. T., Herrmann, C. S. & Huster, R. J. When holding your horses meets the deer in the headlights: time-frequency characteristics of global and selective stopping under conditions of proactive and reactive control. *Front Hum. Neurosci.* **8**, 994 (2014).
50. Green, N. et al. Reduction of influence of task difficulty on perceptual decision making by stn deep brain stimulation. *Curr. Biol.* **23**, 1681–1684 (2013).
51. Nambu, A., Tokuno, H. & Takada, M. Functional significance of the cortico–subthalamo–pallidal 'hyperdirect' pathway. *Neurosci. Res.* **43**, 111–117 (2002).
52. Tan, H. et al. Decoding gripping force based on local field potentials recorded from subthalamic nucleus in humans. *Elife* **5**, 1–24 (2016).
53. Hell, F., Taylor, P. C. J., Mehrkens, J. H. & Bötzel, K. Subthalamic stimulation, oscillatory activity and connectivity reveal functional role of STN and network mechanisms during decision making under conflict. *Neuroimage* **171**, 222–233 (2018).
54. Frank, M. J. Hold your horses: a dynamic computational role for the subthalamic nucleus in decision making. *Neural Netw.* **19**, 1120–1136 (2006).
55. Eisinger, R. S. et al. Parkinsonian beta dynamics during rest and movement in the dorsal pallidum and subthalamic nucleus. *J. Neurosci.* **40**, 2859–2867 (2020).
56. Muralidharan, V., Aron, A. R. & Schmidt, R. Transient beta modulates decision thresholds during human action-stopping. *Neuroimage* **254**, 119145 (2022).
57. Swann, N. et al. Intracranial EEG reveals a time- and frequency-specific role for the right inferior frontal gyrus and primary motor cortex in stopping initiated responses. *J. Neurosci.* **29**, 12675–12685 (2009).
58. Zaepffel, M., Trachel, R., Kilavik, B. E. & Brochier, T. Modulations of EEG beta power during planning and execution of grasping movements. *PLoS One* **8**, e60060 (2013).
59. Wessel, J. R. beta-bursts reveal the trial-to-trial dynamics of movement initiation and cancellation. *J. Neurosci.* **40**, 411–423 (2020).
60. Wagner, J., Wessel, J. R., Ghahremani, A. & Aron, A. R. Establishing a right frontal beta signature for stopping action in scalp EEG: implications for testing inhibitory control in other task contexts. *J. Cogn. Neurosci.* **30**, 107–118 (2018).
61. Pasquereau, B. & Turner, R. S. Neural dynamics underlying self-control in the primate subthalamic nucleus. *Elife* **12**, 1–27 (2023).
62. Patel, S. R. et al. Studying task-related activity of individual neurons in the human brain. *Nat. Protoc.* **8**, 949–957 (2013).
63. Rossi, P. J. et al. The human subthalamic nucleus and globus pallidus internus differentially encode reward during action control. *Hum. Brain Mapp.* **38**, 1952–1964 (2017).
64. Bastin, J. et al. Inhibitory control and error monitoring by human subthalamic neurons. *Transl. Psychiatry* **4**, e439-e439 (2014).
65. Zaghloul, K. A. et al. Neuronal activity in the human subthalamic nucleus encodes decision conflict during action selection. *J. Neurosci.* **32**, 2453–2460 (2012).
66. Zavala, B. et al. Human subthalamic nucleus theta and beta oscillations entrain neuronal firing during sensorimotor conflict. *Cereb. Cortex* **27**, 496–508 (2015).
67. Burbaud, P. et al. Neuronal activity correlated with checking behaviour in the subthalamic nucleus of patients with obsessive-compulsive disorder. *Brain* **136**, 304–317 (2013).
68. Favre, E., Ballanger, B., Thobois, S., Broussolle, E. & Boulinguez, P. Deep brain stimulation of the subthalamic nucleus, but not dopaminergic medication, improves proactive inhibitory control of movement initiation in Parkinson's disease. *Neurotherapeutics* **10**, 154–167 (2013).
69. Pasquereau, B. & Turner, R. S. A selective role for ventromedial subthalamic nucleus in inhibitory control. *Elife* **6**, 1–27 (2017).
70. Lipski, W. J. et al. Subthalamic nucleus neurons differentially encode early and late aspects of speech production. *J. Neurosci.* **38**, 5620–5631 (2018).
71. Wichmann, T. & Soares, J. Neuronal firing before and after burst discharges in the monkey basal ganglia is predictably patterned in the normal state and altered in parkinsonism. *J. Neurophysiol.* **95**, 2120–2133 (2006).
72. Beurrier, C., Congar, P., Bioulac, B. & Hammond, C. *Subthalamic Nucleus Neurons Switch from Single-Spike Activity to Burst-Firing Mode*. (1989).
73. Lévesque, J.-C. & Parent, A. GABAergic interneurons in human subthalamic nucleus. *Mov. Disord.* **20**, 574–584 (2005).
74. Di Caprio, V., Modugno, N., Mancini, C., Olivola, E. & Mirabella, G. Early-stage Parkinson's patients show selective impairment in reactive but not proactive inhibition. *Mov. Disord.* **35**, 409–418 (2020).
75. Micheli, F. et al. Impulsivity markers in Parkinsonian subthalamic single-unit activity. *Mov. Disord.* **36**, 1435–1440 (2021).

76. Hershey, T. et al. Mapping Go-No-Go performance within the subthalamic nucleus region. *Brain* **133**, 3625–3634 (2010).
77. van Wouwe, N. C. et al. Focused stimulation of dorsal subthalamic nucleus improves reactive inhibitory control of action impulses. *Neuropsychologia* **99**, 37–47 (2017).
78. Schuepbach, W. M. M. et al. Neurostimulation for Parkinson's disease with early motor complications. *N. Engl. J. Med.* **368**, 610–622 (2024).
79. Hacker, M. L. et al. Deep brain stimulation in early-stage Parkinson disease. *Neurology* **95**, e393–e401 (2020).
80. Qi, R. et al. Outcomes of STN-DBS in PD patients with different rates of disease progression over one year of follow-up. *Front. Neurol.* **11**, 600 (2020).
81. Kleiner, M. et al. What's new in Psychtoolbox-3. *Perception* **36**, 1–16 (2007).
82. Sanders, J. & Kepecs, A. A low-cost programmable pulse generator for physiology and behavior. *Front. Neuroeng.* **7**, 43 (2014).
83. Andrade-Souza, Y. M. et al. Comparison of three methods of targeting the subthalamic nucleus for chronic stimulation in Parkinson's disease. *Neurosurgery* **62**, 360 (2008).
84. Fischl, B. FreeSurfer. *NeuroImage* **62**, 774–781 (2012).
85. Jenkinson, M., Beckmann, C. F., Behrens, T. E. J., Woolrich, M. W. & Smith, S. M. Fsl. *Neuroimage* **62**, 782–790 (2012).
86. Behrens, T. E. J. et al. Non-invasive mapping of connections between human thalamus and cortex using diffusion imaging. *Nat. Neurosci.* **6**, 750–757 (2003).
87. Hernandez-Fernandez, M. et al. Using GPUs to accelerate computational diffusion MRI: from microstructure estimation to tractography and connectomes. *Neuroimage* **188**, 598–615 (2019).
88. Lio, G., Thobois, S., Ballanger, B., Lau, B. & Boulinguez, P. Removing deep brain stimulation artifacts from the electroencephalogram: issues, recommendations and an open-source toolbox. *Clin. Neurophysiol.* **129**, 2170–2185 (2018).
89. Delorme, A. & Makeig, S. EEGLAB: an open source toolbox for analysis of single-trial EEG dynamics including independent component analysis. *J. Neurosci. Methods* vol. 134 http://www.sccn.ucsd.edu/eeglab/ (2004).
90. Mullen, T. CleanLine EEGLAB plugin. *San Diego, CA: Neuroimaging Informatics Toolsand Resources Clearinghouse (NITRC)* (2012).
91. Winkler, I., Debener, S., Müller, K.-R. & Tangermann, M. *On the Influence of High-Pass Filtering on ICA-Based Artifact Reduction in EEG-ERP*. https://doi.org/10.1109/EMBC.2015.7319296 (2015).
92. Hyvärinen, A. Fast and Robust fixed-point algorithms for independent component analysis. *IEEE Trans. Neural Netw.* **10** (1999).
93. Nunez, P. L. & Pilgreen, K. L. The spline-laplacian in clinical neurophysiology: a method to improve EEG spatial resolution. *J. Clin. Neurophysiol.* **8**, 397–413 (1991).
94. Perrin, F., Bertrand, O. & Pernier, J. Scalp current density mapping: value and estimation from potential data. *IEEE Trans. Biomed. Eng. BME* **34**, 283–288 (1987).
95. Oostenveld, R., Fries, P., Maris, E. & Schoffelen, J. M. FieldTrip: Open source software for advanced analysis of MEG, EEG, and invasive electrophysiological data. *Comput. Intell. Neurosci.* **2011**, 156869 (2011).
96. Waschke, L. et al. Modality-specific tracking of attention and sensory statistics in the human electrophysiological spectral exponent. https://doi.org/10.7554/eLife.
97. Perrin, F., Pernier, J., Bertrand, O. & Echallier, J. F. Spherical splines for scalp potential and current density mapping. *Electroencephalogr. Clin. Neurophysiol.* **72**, 184–187 (1989).
98. The MathWorks Inc. *MATLAB version R2019b*. (Natick, MA: The MathWorks Inc., 2019).
99. Farge, M. Wavelet transforms and their applications to turbulence. *Annu. Rev. Fluid Mech.* **24**, 395–457 (1992).
100. Torrence, C. & Compo, G. P. A practical guide to wavelet analysis. *Bull. Am. Meteorol. Soc.* **79**, 61–78 (1998).
101. Grandchamp, R. & Delorme, A. Single-trial normalization for event-related spectral decomposition reduces sensitivity to noisy trials. *Front Psychol.* **2**, 236 (2011).
102. Hangya, B., Ranade, S. P., Lorenc, M. & Kepecs, A. Central cholinergic neurons are rapidly recruited by reinforcement feedback. *Cell* **162**, 1155–1168 (2015).
103. Rossant, C. et al. Spike sorting for large, dense electrode arrays. *Nat. Neurosci.* **19**, 634–641 (2016).
104. Schmitzer-Torbert, N., Jackson, J., Henze, D., Harris, K. & Redish, A. D. Quantitative measures of cluster quality for use in extracellular recordings. *Neuroscience* **131**, 1–11 (2005).
105. Kim, J. et al. Inhibitory basal ganglia inputs induce excitatory motor signals in the Thalamus. *Neuron* **95**, 1181–1196.e8 (2017).
106. Tekriwal, A., Lintz, M. J., Thompson, J. A. & Felsen, G. Disrupted basal ganglia output during movement preparation in hemiparkinsonian mice is consistent with behavioral deficits. *J. Neurophysiol.* **126**, 1248–1264 (2021).
107. Hegedüs, P., Sviatkó, K., Király, B., Martínez-Bellver, S. & Hangya, B. Cholinergic activity reflects reward expectations and predicts behavioral responses. *iScience* **26**, 105814 (2023).
108. Hegedüs, P. et al. Parvalbumin-expressing basal forebrain neurons mediate learning from negative experience. *Nat. Commun.* **15**, 4768 (2024).
109. Nambu, A., Takada, M., Inase, M. & Tokunoz, H. Dual somatotopical representations in the primate subthalamic nucleus: evidence for ordered but reversed body-map transformations from the primary motor cortex and the supplementary motor area. *J. Neurosci.* **16**, 2671–2683 (1996).
110. Szabo, J. P. et al. Dataset for 'Neurons of the human subthalamic nucleus engage with local delta frequency processes during action cancellation'. Figshare https://doi.org/10.6084/m9.figshare.31359616 (2026).
111. Szabó, J. P., Laszlovszky, T., Király, B. & Hangya, B. kiralyb/human-STN-delta: Human-STN-delta. Final release for Szabó et al., 2026, Nat Comm (v1.0). *Zenodo* https://github.com/kiralyb/human-STN-delta, https://doi.org/10.5281/zenodo.18679923 (2026).

Acknowledgements

We thank prof. Dániel Bereczki for his support of the project. This work was supported by the Hungarian Brain Research Program NAP3.0 (NAP2022-I-1/2022) of the Hungarian Academy of Sciences and the ERC POC grant 101123104 to B.H.

Author contributions

B.H. designed and supervised the research and acquired funding; P.H., T.L., J.P.S. and B.H. performed experiments with help from G.P., V.B., G.T. and D.F; L.Er., L.H. and L.En. implanted electrodes; L.H. and G.M. reconstructed electrode trajectories; T.L. and I.U. designed research tools; G.T. recruited study participant; J.P.S., B.K. and B.H. analyzed the data; J.P.S. and B.H. discussed the results and wrote the paper; all authors reviewed and revised the final manuscript.

Competing interests

The authors declare the following competing interests: B.H. and T.L. are listed as a co-inventors on the approved Hungarian utility model U2200127, pending Hungarian patent application P2200356 and pending PCT PCT/HU2023/050054 seeking to protect the custom-designed button box used in this study. The other authors declare no competing interests.

Additional information

Supplementary information The online version contains supplementary material available at https://doi.org/10.1038/s41467-026-71502-z.

Correspondence and requests for materials should be addressed to Balázs Hangya.

Peer review information *Nature Communications* thanks Ueli Rutishauser (eRef) who co-reviewed with Clayton Mosher (ECR), and the other anonymous reviewer(s) for their contribution to the peer review of this work. A peer review file is available.